



Cite this: *EES Catal.*, 2026, 4, 55

## Beyond activity: a perspective on diagnosing instability of reversible O<sub>2</sub> catalysts for metal–air batteries

Ricardo P. M. Duarte,<sup>id bc</sup> Reshma R. Rao,<sup>id b</sup> Mary P. Ryan,<sup>b</sup> Trung Dung Tran,<sup>a</sup> Veronica Celorrio,<sup>id d</sup> Jonathan Sharman,<sup>a</sup> Alex M. Bonastre<sup>\*a</sup> and Ifan E. L. Stephens<sup>id \*b</sup>

Zinc–air redox flow batteries have high potential to penetrate the stationary energy storage market, due to the abundance, and low cost of active species – oxygen and zinc. However, their technological fruition is limited by the development of reversible O<sub>2</sub> electrodes operating at potentials between 0.6 V<sub>RHE</sub> to 1.7 V<sub>RHE</sub>, under which no catalyst material has been shown to be stable over long durations. Despite heavy research on the topic of reversible O<sub>2</sub> catalysis, little is known about the parameters controlling the stability of the bifunctional catalyst. Several research accounts assess the activity of reversible O<sub>2</sub> catalysts, but only a small portion cover degradation mechanism over such a large potential window. In this perspective, we summarize our current understanding of material challenges for Zn–air batteries, reversible O<sub>2</sub> catalyst integration strategies, and electrochemical behaviour, with a particular focus on catalyst stability. Nickel cobalt oxide (NiCo<sub>2</sub>O<sub>4</sub>), a promising yet understudied system, is used as an example material for investigations at potentials of both the O<sub>2</sub> reduction (ORR) and evolution (OER) reactions. We also report original data employing *ex situ* X-ray diffraction, electron energy loss spectroscopy, and X-ray photoelectron spectroscopy, as well as electrochemical measurements to study the activity of NiCo<sub>2</sub>O<sub>4</sub>. Furthermore, electrochemical accelerated stress tests are coupled with post-mortem transmission electron microscopy, inductively coupled plasma, and X-ray photoelectron spectroscopy to study the dissolution, compositional changes and amorphization of the top surface 5 nm of the catalyst surface. *In situ* X-ray absorption spectroscopy revealed irreversible oxidation of Co centres in NiCo<sub>2</sub>O<sub>4</sub> during OER, which explains the reduction in activity of the ORR after the catalyst was exposed to anodic OER potentials. This methodology provides a broader method to screen reversible O<sub>2</sub> catalyst stability and enables us to summarize future strategies to improve the activity and stability of reversible O<sub>2</sub> catalysts and electrodes.

Received 1st August 2025,  
Accepted 17th September 2025

DOI: 10.1039/d5ey00236b

rsc.li/eescatalysis

### Broader context

Reliable access to on-demand energy is key to societal development. However, electricity generation accounts for almost 50% of all CO<sub>2</sub> emissions, and the aging grid does not have the capacity to accommodate the required increases in renewable resources; their intermittent nature calls for the development of large-scale electric energy conversion and storage systems such as pumped hydro, compressed air or batteries. Batteries are the most promising solution since they do not require pre-existing geological features. Zinc–air batteries have a high potential to penetrate the stationary energy storage market, since their active species – O<sub>2</sub> and Zn – and aqueous chemistry make them cost efficient, quickly deployable, and environmentally friendly. However, no catalyst material has been shown to survive the harsh potentials at which the air electrode operates: 0.6 V<sub>RHE</sub> to 1.7 V<sub>RHE</sub>. NiCo<sub>2</sub>O<sub>4</sub> is a good candidate for this application because it is active for the O<sub>2</sub> reduction and evolution reactions, and its elements are thermodynamically stable at anodic potentials. However, the subject of long-term durability at such large potential windows is subject of little attention, and is key to the technological fruition of Zn–air batteries.

## 1. Introduction

### 1.1. Rechargeable zinc–air batteries for large scale energy storage

Stationary energy storage devices have the potential to reduce global CO<sub>2</sub> emissions by almost 50%, if the electricity and heat generation sectors are made fully reliant on renewables.<sup>1,2</sup>

<sup>a</sup> Johnson Matthey Technology Center, Reading, RG4 9NH, UK

<sup>b</sup> Department of Materials, Royal School of Mines, Imperial College London, London, SW7 2AZ, UK. E-mail: i.stephens@imperial.ac.uk

<sup>c</sup> Chemistry and Nanoscience center, National Renewable Energy Laboratory, Golden, CO, 80401, USA

<sup>d</sup> Diamond Light Source, Harwell Science and Innovation Campus, Didcot OX11 0DE, UK



Pumped hydro and compressed air are the only technologies mature enough to provide bulk energy management services, such as energy time shift, and supply capacity.<sup>3</sup> Electrochemical energy storage devices such as Li-ion, lead-acid and flow batteries show promise to upgrade the electrical grid due to their ability to be directly coupled with renewables.<sup>4–6</sup> Li-ion, and lead acid batteries are the most widely used chemistries due to their high round trip efficiency and have seen grid-level application.<sup>7</sup> However, their widespread application to large scale energy storage is limited by their low durability, and scalability issues.<sup>8,9</sup> Flow batteries are a promising strategy to employ such electrochemical energy storage devices at the TW scale since power

and capacity can be scaled independently. This feature allows application to a wider range of scenarios without compromising cost. Many chemistries can be employed in this configuration with the most mature ones being vanadium, and Zn–Br batteries.<sup>10,11</sup> Although total installed flow battery power and capacity comprises 5–10% of that of Li-ion,<sup>4</sup> commercial projects up to 100 MW and 400 MWh have been installed showing its promise in large scale storage.<sup>12</sup> However, even though these technologies have matured significantly over the years, they still lack the necessary specifications to be applied at such large scales. Zn–air batteries are a promising technology to fulfil this role, if their rechargeability issues are solved.



**Ricardo P. M. Duarte**

*Ricardo P. M. Duarte is a Post-doctoral researcher at the National Renewable Energy Laboratory. He obtained his PhD from Imperial College London in 2023, conducting his research full-time at Johnson Matthey as a Marie-Sklodowska Curie fellow within the FLOWCAMP project. Following his doctorate, he continued at Johnson Matthey as a Staff Scientist before joining NREL. His research focuses on advancing the safety and efficiency of proton exchange membrane water electrolysis, with particular emphasis on high-pressure operation.*



**Reshma R. Rao**

*Reshma Rao is an Assistant Professor at the Grantham Institute – Climate Change and the Environment and the Department of Materials, Imperial College London. Since 2022, she also holds a Royal Academy of Engineering Research Fellowship. Reshma obtained her PhD from the Massachusetts Institute of Technology in 2019, and was a research associate in the Department of Chemistry and the Department of Materials at Imperial College from 2020 to 2022. She now leads her own independent group. Her research interests include understanding (electro)chemical reactivity at solid-gas and solid-liquid interfaces in order to develop more active, stable and selective catalysts for electrochemical technologies that can produce renewable fuels and chemicals.*



**Alex M. Bonastre**

*Alexandro Martinez Bonastre, received his PhD from Southampton University, UK, in 2007 and joined the Fuel Cells Research Group at Johnson Matthey Technology Centre, Sonning Common, UK, in 2006 as research scientist. He currently leads the R&D hydrogen fuel cells team and his work centers on the electrochemical characterisation of catalysts and fuel cell components. He is a technical leader in the areas of alcohol and hydrogen fuel cells, working mostly with platinum group metal catalysts.*

*Alexandro Martinez Bonastre, received his PhD from Southampton University, UK, in 2007 and joined the Fuel Cells Research Group at Johnson Matthey Technology Centre, Sonning Common, UK, in 2006 as research scientist. He currently leads the R&D hydrogen fuel cells team and his work centers on the electrochemical characterisation of catalysts and fuel cell components. He is a technical leader in the areas of alcohol and hydrogen fuel cells, working mostly with platinum group metal catalysts.*



**Ifan E. L. Stephens**

*Ifan Stephens is Professor of Electrochemistry in the Department of Materials at Imperial College London. His research focuses on understanding and optimizing electrocatalytic reactions at the molecular level, with applications in sustainable energy conversion and storage. He leads the Interfacial Electrochemistry Group and is Research Area Lead for “Atoms to Devices” within the Henry Royce Institute. A co-founder of HPNow, he has authored over 130 publications on topics including oxygen, nitrogen, hydrogen, and carbon electrochemistry, combining electrochemical methods, synthesis and characterization to address key challenges in catalyst design and deployment.*

*Ifan Stephens is Professor of Electrochemistry in the Department of Materials at Imperial College London. His research focuses on understanding and optimizing electrocatalytic reactions at the molecular level, with applications in sustainable energy conversion and storage. He leads the Interfacial Electrochemistry Group and is Research Area Lead for “Atoms to Devices” within the Henry Royce Institute. A co-founder of HPNow, he has authored over 130 publications on topics including oxygen, nitrogen, hydrogen, and carbon electrochemistry, combining electrochemical methods, synthesis and characterization to address key challenges in catalyst design and deployment.*





Fig. 1 Schematic illustration of the components in a redox flow battery. Catholyte and anolyte correspond to the compartments where the active species with more cathodic, or anodic half-cell potentials are stored.

Batteries for large scale grid storage require durability for large numbers of cycles, high round trip efficiencies, and employment of scalable active species that are abundant and recyclable. Li-ion, and lead acid batteries are the most widely used chemistries due to their high round trip efficiency and have seen some grid-level application. However, their widespread application to large scale energy storage is limited by their low durability, and scalability issues. Flow batteries, schematized in Fig. 1 are a promising strategy to employ such electrochemical energy storage devices at the TW scale. Since the system's power and capacity can be scaled independently, it can be tailored for a wider range of scenarios without compromising cost. Many chemistries can be employed in this configuration with the most mature ones being vanadium, and Zn–Br batteries.<sup>10,11</sup>

Zn–air batteries are a promising chemistry to accomplish an even cheaper and more scalable battery technology employing environmentally friendly and abundant components.<sup>7,13,14</sup> When compared to competing battery technologies, Zn–air batteries have a high theoretical energy density of  $1352 \text{ Wh kg}_{\text{Zn}}^{-1}$ . One of the active species  $-\text{O}_2-$  is inexhaustible as it can be harvested from atmospheric air which can be directly fed into the system. Metrics to assess the scalability of different active species, relating abundance and electrochemical properties, are currently lacking in literature. Herein, we use the world mineral production,<sup>15</sup> while considering perfect storage capacity, to estimate how long it would take to mine active species to fulfil 1 TWh. Fig. 2 shows the estimated material extraction time per unit energy for the different battery technologies. Alongside, are shown cost projections made by the US department of energy for bulk energy services.<sup>7</sup>

A theoretical value of 25 days of zinc extraction time per TWh is estimated for zinc–air, which is not matched by

competing technologies. In addition, the DOE's cost projections also indicate that Zn–air can be one of the cheapest technologies to scale up.<sup>7</sup> This analysis also shows that zinc–air flow batteries could have a very fast deployment capacity, which could be desirable in emergency events, such as fossil fuel shortage. In addition, the recyclability of Zn also allows for easy maintenance of the deployed capacity once battery lifetime has been surpassed. In practice, Zn–air batteries are still at low technology readiness levels, which limit their application to large scale energy storage. To the best of our knowledge, the most technologically mature instance of Zn–air batteries, designed for grid-scale operation, was a flow assisted 1 kW–4 kWh system.<sup>19</sup> In this project, it was identified that the main challenges for scale up are: the need for using two separate electrodes to catalyze the oxygen reduction (ORR) and evolution reaction (OER), electrolyte leakage, and flooding of the air electrode.<sup>19</sup> In the following section, we summarize the current challenges associated with each of the components in Zn–air batteries, and strategies to improve their performance.

## 1.2. Rechargeable zinc–air batteries: challenges and mitigation strategies

The reactions taking place at the air–electrode and zinc electrode are shown in eqn (1.1) and (1.2), respectively. Upon discharge, oxygen and zinc are consumed to yield soluble zincate  $\text{Zn}(\text{OH})_4^{2-}$  which is then followed by the precipitation of insulating zinc oxide (ZnO) when zincate saturation is achieved, as shown in eqn (1.3). In rechargeable zinc–air batteries, these reactions are reversed to regenerate metallic zinc, by electrodeposition of dissolved  $\text{Zn}(\text{OH})_4^{2-}$ , as oxygen and water are generated at the air–electrode. The reactions occurring at the air–electrode during charge and discharge, respectively, are called the oxygen evolution reaction (OER) and the oxygen reduction reaction (ORR).



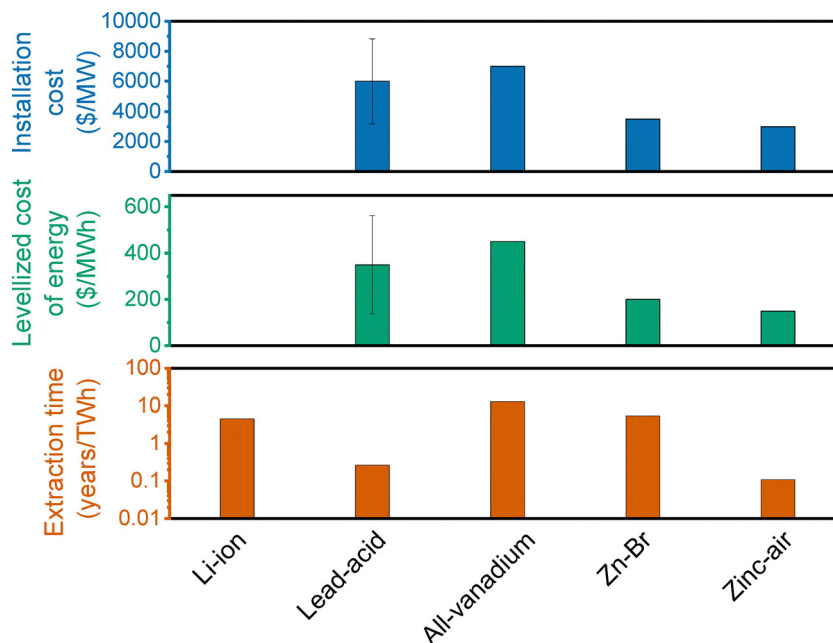
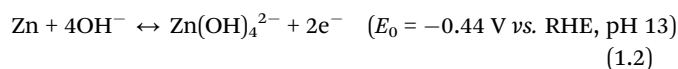


**Fig. 2** Time required to extract the redox active components to reach an energy content of 1 TWh, based on the theoretical full-cell voltages, while assuming 100% battery efficiency. Energy per mol reactants was calculated from  $\Delta G^0 = -nFE^0$ , where  $n$  is the number of electrons transferred,  $F$  is Faraday's constant ( $96485 \text{ C mol}^{-1}$ ) and  $E^0$  is the theoretical cell voltage. Energy per mass of active species is a conversion from  $\text{kJ mol}_{\text{reactants}}^{-1}$  to  $\text{Wh kg}_{\text{active species}}^{-1}$ , assuming that only metallic, and carbon species contribute to the weight of each half-cell. This excludes oxygen for zinc-air batteries which is readily available in the atmosphere. Material extraction time per TWh was calculated by dividing the mass of active components required for 1 TWh by its world annual production. Worldly annual mineral production was extracted from the year of 2021 in the 2017–2021 British Geological Survey's world mineral production.<sup>15</sup> Graphite anode Li-ion batteries were taken into account with a cell potential of 3.7 V as reported by Eftekhari.<sup>16</sup> Co, Li and graphite extraction times were estimated by taking the one electron transfer, full-cell reaction into account:  $\text{LiCoO}_2 + 6\text{C} \leftrightarrow \text{CoO}_2 + \text{LiC}_6$ , leading to 42.4 wt% C, 34.6 wt% Co, 4 wt% Li and 19 wt% O. It is noted that oxygen was not taken into account for the material extraction time per TWh as metallic cobalt extraction per year is given in ref. 17. Full cell voltages of 2.04 V were assumed for the lead acid system ( $\text{PbO}_2 + \text{Pb} \leftrightarrow \text{H}_2\text{O} + 2\text{PbSO}_4$ ),<sup>18</sup> 1.26 V for the All-vanadium system ( $\text{V}^{3+} + \text{VO}^{2+} + \text{H}_2\text{O} \leftrightarrow \text{VO}_2^+ + \text{V}^{2+} + 2\text{H}^+$ ),<sup>10</sup> 1.82 V for the zinc-bromine system ( $\text{Zn} + \text{Br}_2 \leftrightarrow \text{Zn}^{2+} + 2\text{Br}^-$ )<sup>10</sup> and 1.65 V for the zinc-air system ( $\text{Zn} + 2\text{H}_2\text{O} + \text{O}_2 \leftrightarrow \text{Zn(OH)}_4^{2-}$ ).<sup>13</sup> Installation cost and levelized cost of energy extracted from the "Energy storage Technology and cost characterization report" facilitated by the U.S. Department of Energy.<sup>7</sup>



During discharge, reversible air-electrodes rely on the formation of a three-phase boundary between the electrolyte, catalyst particles, and supply gas to catalyse the ORR. Such condition is not required during OER, where a flooded catalyst layer is beneficial to maximize access to the electrolyte. For the ORR and OER to take place, the catalyst also needs to be electrically connected to the external circuit, which is made through the gas diffusion layer.

The different possible zinc-air battery architectures are also schematized in Fig. 3. Primary zinc-air batteries employ a static electrolyte, a separator impregnated with aqueous alkaline solution is sandwiched between a metallic zinc electrode and an air electrode. Such configuration employs an air-electrode with a single component catalyst layer comprising of an ORR active material held together by a polymeric binder and supported on a porous conductive substrate (*i.e.* Ni screen).<sup>20,21</sup>

When reversing the reactions, other configurations such as a flowing KOH electrolyte,<sup>19,22,23</sup> or a flowing slurry of Zn particles suspended in the alkaline electrolyte<sup>24–26</sup> are beneficial. In Zn-air batteries, power is determined by the area and efficiency of the stack (*i.e.* Zn and air electrode assembly), whereas capacity is determined by the total amount of Zn in the battery. It is worth mentioning that a zinc-slurry configuration is the first documented Zn-based flow battery to enable the decoupling of power and capacity. The capacity of other flow-assisted configurations is always limited by the amount of Zn that can be electrodeposited at the Zn electrode.

At the air-electrode, different configurations are also possible due to the need of catalysing both ORR and OER. A single electrode configuration can be used, where either a single catalyst is used to catalyze the two reactions,<sup>27–29</sup> or two different components are used to catalyze both ORR and OER.<sup>30,31</sup> As illustrated in Fig. 3, two different components can be integrated in either a layered structure<sup>22,32</sup> or in a single multi-component catalyst layer.<sup>30,31</sup> The bi-electrode configuration can be used where the ORR and OER electrodes are kept at open circuit during charge and discharge respectively.<sup>19,33</sup> In practice, charge and discharge can also be done in different modules.<sup>24,34</sup> Even though such solution could achieve most





Fig. 3 Schematic illustration of zinc–air battery architecture and its different possible configurations.

promising stabilities, it increases the mechanical complexity of the system, and will not be covered extensively in this perspective paper. Table 1 summarizes the main challenges associated with the zinc–air chemistry, and strategies to mitigate them. Some of such solutions include different configurations shown in Fig. 3. The main issues occurring at the zinc electrode are passivation during discharge, dendrite growth during charge, spontaneous Zn corrosion and parasitic H<sub>2</sub> evolution reaction (HER) during charge cycles.<sup>35,36</sup> Zn corrosion accompanied by HER occurs because Zn/Zn(OH)<sub>4</sub><sup>2-</sup> has a lower equilibrium potential than H<sub>2</sub>/OH<sup>-</sup>.<sup>37</sup> This necessitates development of strategies to inhibit HER<sup>38–41</sup> increase shelf-life and safety by inhibiting corrosion and preventing the formation of an explosive atmosphere. At the same time, decreasing HER increases charging efficiency by preventing such a parasitic reaction, which can be achieved by alloying Zn,<sup>38–40</sup> employing coatings,<sup>42,43</sup> or using neutral electrolytes which increase the equilibrium potential of Zn/Zn(OH)<sub>4</sub><sup>2-</sup>.<sup>37,44</sup>

Passivation occurs when discharging at mass transport limited currents due to the concentration of Zn(OH)<sub>4</sub><sup>2-</sup> rising

above the solubility limit at the electrode interface.<sup>35</sup> Discharging at low current densities provides a short-term solution to prevent the formation of ZnO.<sup>47</sup> However, operating electrochemical devices at higher current densities is desirable since it allows for more flexible operation to offset varying renewable loads. Increasing zincate solubility, *via* increasing KOH molarity<sup>47</sup> or electrolyte additives,<sup>48</sup> and flowing the electrolyte<sup>23</sup> are among the best strategies to retard the precipitation of ZnO. These increasing the diffusion of zincate away from the electrode interface.

Dendrite growth is one of the main problems when charging Zn–air batteries, occurring mainly at mass transport limited current densities.<sup>35,65</sup> The depletion of zincate ions at the surface lead to the preferential deposition of metallic zinc at protruding areas of the electrode, where the Zn(OH)<sub>4</sub><sup>2-</sup> diffusion path is shorter, and the local ohmic drops are lower. Ultimately, dendrites can grow to create an electrically conductive path across the electrolyte leading to catastrophic failure by short-circuit.<sup>19</sup> Among strategies to prevent this event are the employment of flowing electrolytes,<sup>19,25,26,47</sup> and electrolyte

Table 1 Summary of challenges and mitigation strategies associated with the different components present in a zinc–air battery

Component	Challenge	Mitigation strategy
Zinc electrode	Zn corrosion, and H <sub>2</sub> evolution Passivation Dendrite growth	Zn alloying, <sup>38–40,45</sup> coatings, <sup>42,43</sup> neutral electrolytes, <sup>37,44</sup> and electrolyte additives <sup>41,46</sup> Increase Zn(OH) <sub>4</sub> <sup>2-</sup> solubility, discharging at low current density, flowing electrolyte, <sup>23,47,48</sup> Flowing electrolyte, <sup>49,50</sup> electrolyte additives, <sup>51,52</sup> polymer separator, flowing Zn slurry; <sup>26</sup>
Electrolyte	CO <sub>2</sub> uptake and HCO <sub>3</sub> <sup>-</sup> precipitation Zincate crossover Ohmic losses	CO <sub>2</sub> trap at air electrode inlet, <sup>19,53</sup> modified electrolytes <sup>49,54–56</sup> Selective AEM, modified porous separator <sup>57,58</sup> Decrease inter-electrode gap, optimized catalyst coated membrane <sup>59</sup>
Air electrode	Flooding GDL corrosion Catalyst efficiency losses	Adequate microporous layer design, <sup>60,61</sup> Bi-electrode configuration <sup>19,33</sup> Gas diffusion layer material selection <sup>62,63</sup> Mixing ORR and OER active materials, <sup>30,64</sup> Bi-electrode configuration <sup>19,33</sup>



additives<sup>51,52</sup> to promote the diffusion of  $\text{Zn}(\text{OH})_4^{2-}$  to the electrode interface. Increasing the solubility of zincate (*i.e.* with additives<sup>51,52</sup> or higher KOH molarity<sup>47</sup>) is likely the best strategy as it prevents both dendrite formation and Zn passivation. Mechanically robust separators such as polymer gels<sup>49,58</sup> or anion exchange membranes<sup>57</sup> can also be employed, possibly avoiding dendrites penetrating through the electrolyte. Another promising strategy is to employ a flowing Zn slurry, which can promote particle collision and dendrite break-up, as well as a higher amount of available surface area for Zn electrodeposition.<sup>25,26</sup>

The alkaline electrolyte is responsible for electrically insulating the Zn and  $\text{O}_2$  electrodes while making ionic contact (*i.e.*  $\text{OH}^-$  transport) between them. The main issues with this component are excessive contribution to cell resistance, *via* Ohmic losses, which prohibit operation at higher current densities.<sup>25,26</sup> Ohmic losses can increase even further when the electrolyte is exposed to atmospheric  $\text{CO}_2$  due to the formation of carbonate anions which have a lower conductivity than  $\text{OH}^-$ .<sup>58,66,67</sup> Over time, the uptake of  $\text{CO}_2$  can lead to the precipitation of carbonate species which clog the air electrode, and lead to catastrophic cell failure.<sup>68</sup> Strategies to avoid such an issue include using neutral electrolytes<sup>55</sup> or ionic liquids<sup>69</sup> but these are likely to result in higher ohmic drops and possibly worse  $\text{O}_2$  catalyst kinetics. It is possible to engineer the battery so that  $\text{CO}_2$  is filtered out of the air electrode feed, which is likely the best strategy.<sup>19,68</sup> Zincate crossover has been mentioned as a possible issue, where  $\text{ZnOH}_4^{2-}$  ions could diffuse to the air-electrode and poison catalyst activity.<sup>57,58</sup> However, to the best of our knowledge, the impact of this contaminant on catalyst activity is still poorly understood.

Anion exchange membranes (AEM) are a promising strategy to improve the operation of Zn-air battery electrolytes.<sup>57,58</sup> Few studies have achieved promising results with such configuration, and we aim to scrutinize their application in large scale storage. Historically proton exchange membranes (PEM) are responsible for allowing fuel cells and electrolyzers to operate efficiently at higher current densities up to 2–5  $\text{A cm}^{-2}$ .<sup>70,71</sup> Similarly to PEM in water electrolysis, AEMs could allow operation at higher current densities when applied to Zn-air batteries. Operating at higher currents is possible due to lower Ohmic losses because of a lower inter electrode gap<sup>72</sup> and excellent bonding between catalyst layer and electrolyte.<sup>59</sup> Operating at higher current densities could enable smaller, and cheaper stack assemblies, at the same power output, especially when expensive raw materials such as Pt and Ir are used (*i.e.* in PEM electrolysis).<sup>73</sup> However, the alkaline chemistry already avoids the use platinum group metal (PGM) catalysts, thus smaller cost reductions are achieved by reducing stack size.<sup>10,73</sup> At the same time, operating at higher current densities would also incur severe round-trip efficiency losses because of the high ORR/OER overpotentials due to lack of optimized air electrode structure.<sup>13,61</sup> Therefore, it might be acceptable to operate at low current densities with larger stack sizes, and thus the decreased need for AEMs in Zn-air flow.

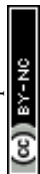
Technoeconomic analysis studies would be needed to clarify the interplay between such variables.

The PEM configuration allowed reducing the weight of fuel cells to be applied to vehicles, whose weight determines their economic feasibility.<sup>74,75</sup> In electrolyzers, ion exchange membranes allowed operating at higher cathode partial pressures with lower  $\text{H}_2$  crossover rates, reducing the cost of compressing hydrogen.<sup>76,77</sup> Zn-air flow batteries are likely to be stationary where its weight is irrelevant, operate at atmospheric pressure, and ambient temperature,<sup>19,26</sup> and it is unclear whether zincate crossover results in catalyst deactivation. Even though no studies exist on such a phenomena, AEMs could mitigate zincate crossover.<sup>57</sup> As disadvantages, AEMs are also poisoned by  $\text{CO}_2$ , which would still need to be filtered,<sup>57,58</sup> and their stability is still lacking.<sup>58</sup> Nonetheless, they still prove to be a promising strategy to improve efficiency, if durable and inexpensive AEMs were developed that could withstand the corrosive environment of 6–8 M KOH.

Reversible air electrodes are mainly limited by flooding,<sup>60,61</sup> and efficiency losses arising from catalysis of  $\text{O}_2$  reduction and evolution reactions.<sup>78,79</sup> Flooding renders  $\text{O}_2$  consuming electrodes inactive and can be minimized by using a gas diffusion layer incorporating a hydrophobic microporous layer.<sup>61</sup> On the other hand,  $\text{O}_2$  evolving electrodes best operate under flooded conditions making it impossible to optimize both ORR and OER in a reversible air electrode. State-of-the-art Zn-air batteries employ a bi-electrode configuration where separate electrodes are used to catalyse the ORR and OER.<sup>19</sup> This approach allows easier optimization of each electrode and increases catalyst stability by keeping the ORR active material at open circuit during charge cycles and *vice versa*. However, such a layout increases the mechanical complexity of the system and increases overall capital cost.<sup>19</sup> The industrial development of these devices is limited by efficient electrodes able to efficiently catalyse both the  $\text{O}_2$  reduction (ORR) and evolution reactions (OER).  $\text{O}_2$  bubble formation can also have an effect on electrode performance during charge cycles. However, this is thought to occur at high current densities above 1  $\text{A cm}^{-2}$ ,<sup>72</sup> a state under which zinc-air flow batteries are unlikely to operate at.

Corrosion of the gas diffusion layer material during OER polarization can compromise device durability.<sup>61,62</sup> The GDL acts as a current collector, and its corrosion/passivation can compromise its electrical conductivity. In PEM water electrolysis, Ti materials coated in Pt are employed<sup>80,81</sup> whereas Ni or stainless steel based porous structures are used in AEM electrolysis.<sup>82,83</sup> Typical carbonaceous materials used in fuel cells employing a microporous layer are more mature but degrade at anodic potentials and hence are unsuitable for  $\text{O}_2$  evolution conditions.<sup>62,63</sup> Thus, reversible air electrodes would ideally require a metallic and hydrophobic microporous layer that would be corrosion resistant and immune to flooding.<sup>61,62,84</sup>

Scaling relations between the binding energetics of reaction intermediates limit the round-trip efficiency of OER/ORR catalysts.<sup>79</sup> In short, lower overpotentials towards one of the reactions come at the cost of higher overpotentials towards the



reverse reaction in a double volcano relationship.<sup>79,85,86</sup> To circumvent this issue, researchers typically employ two different active components which catalyse each of the reactions separately.<sup>30,64,87</sup> Typically, N-doped carbons are mixed with transition metal oxides which are active towards the ORR and OER respectively. However, carbon corrodes at OER potentials and thus there is a drive to develop carbon-free reversible O<sub>2</sub> electrodes.<sup>62,63,88</sup> A possible route to accomplish stable reversible O<sub>2</sub> electrodes is to find a single catalyst material that is active and stable for both ORR and OER.<sup>27,61</sup>

Several research accounts review the challenges associated with each of the components: the zinc electrode,<sup>35</sup> the alkaline electrolyte,<sup>49,58</sup> and air-electrode.<sup>13,89–91</sup> However, the stability of reversible O<sub>2</sub> catalysts, one of the most challenging issues to solve, has been largely overlooked. In other words, electrochemical stability is often assessed based on improvements in short term accelerated stress tests in demonstration scale devices.<sup>27,92,93</sup> However, direct evidence of suppressed dissolution products such as metal cations<sup>94–96</sup> or CO, CO<sub>2</sub> and carbonates,<sup>88,97,98</sup> is necessary to use device scale testing to qualify long term operation over the span of several years.<sup>99</sup> The few papers addressing the degradation of ORR/OER catalysts are limited to dissolution of Mn based oxides which are far too unstable to be of practical usage.<sup>94,96</sup> The evidence thus far suggests that we have not discovered catalysts that are stable against dissolution or other forms of degradation under both O<sub>2</sub> evolution and O<sub>2</sub> reduction conditions.<sup>95,100,101</sup> In the next section, we summarize the current knowledge relating to ORR and OER catalyst activity and stability. Motivated by decreasing installation cost by having a single reversible air-electrode, we focus on finding a single component catalyst that can catalyze the ORR and OER. In addition, due to the unstable nature of carbonaceous materials,<sup>63,88,97</sup> we focus on transition metal oxides as the most promising class of materials to fulfil this role.

## 2. State-of-the-art reversible O<sub>2</sub> catalysts for zinc–air batteries

Vanadium redox flow batteries are likely the closest competitor to rechargeable zinc–air redox flow batteries.<sup>3,102</sup> Thus, it is likely that reversible air electrodes would have to operate at around 100–400 mA cm<sup>-2</sup>, round trip efficiencies of about 75–90% and lifetimes between 10–30 years.<sup>3,10</sup> While no studies exist employing reference electrodes, an optimistic scenario of a reversible air electrode operation can be drawn. At around 150 mA cm<sup>-2</sup> it is possible to operate optimized PEM fuel cell cathodes at around 0.85 V<sup>103</sup> and electrolyser anodes at 1.5 V at 80 °C.<sup>72</sup> Such values would yield round trip efficiencies of close to 60%, assuming no losses from the zinc electrode. Such an observation highlights the need to develop reversible O<sub>2</sub> catalysts with higher electrocatalytic activity than benchmarked Pt and Ir catalysts, as well as electrodes optimized to both ORR and OER. Furthermore, in practice, reversible electrodes are likely to operate in a voltage window between 0.6 V<sub>RHE</sub> and 1.7

V<sub>RHE</sub>, under which no material has been shown to be stable.<sup>94,96</sup> This issue is largely overlooked in literature, given that an electrode would have to maintain at least 10 years of operation under such conditions. Such conditions lay the design targets for bifunctional O<sub>2</sub> catalysts for Zn–air batteries.

### 2.1. Activity of reversible O<sub>2</sub> catalysts

Non-precious metal oxides, based on abundant elements such as Ni, Co and Fe, are the most promising class of materials to be employed in alkaline-based devices.<sup>104</sup> In principle, catalyst loading should be maximised as much as possible without imposing transport limitations.<sup>105,106</sup> The situation contrasts with platinum group metal (PGM) catalysts, where the high cost of Pt/C catalysts for O<sub>2</sub> reduction and IrO<sub>x</sub> for O<sub>2</sub> evolution constrains the practical loading.<sup>105</sup> Gasteiger *et al.* argue that a non-precious metal ORR catalyst qualifies as a potential candidate for automotive fuel cells if its intrinsic activity allows to match the activity of an electrode with 0.4 mg<sub>Pt</sub> cm<sup>-2</sup>.<sup>105,106</sup> Assuming no loading effects below a catalyst layer thickness of 100 μm, a maximum catalyst loading along with a projected activity can be estimated based on mass activities determined *via* rotating disk electrode (RDE).<sup>105</sup> Reversible air electrodes are bound to experience worse catalyst utilization at higher loadings due to the difficulty of optimizing the three-phase boundary towards the two reactions. Maximizing the geometric activity of an electrode then becomes a different problem to that of increasing catalyst intrinsic activity. For example, NiFeOOH has higher intrinsic activity than IrO<sub>x</sub>, and is the most active OER catalyst in alkaline media.<sup>107–109</sup> Nonetheless, studies found IrO<sub>x</sub> to be more active when applied at higher loadings in a device configuration, likely due to its higher conductivity.<sup>110</sup> Thus, we propose that the intrinsic activity of IrO<sub>x</sub> is used as a target for OER activity of bifunctional catalysts for reversible air electrodes, as shown in Fig. 4. In summary, we suggest that researchers focus on matching the intrinsic activity of bifunctional catalysts as a separate question to reaching high geometric currents. Pt and IrO<sub>x</sub> can serve as an initial intrinsic activity target that needs to be matched to achieve higher than 60% round trip efficiencies.

Among the most active carbon-free O<sub>2</sub> bifunctional catalysts are transition metal oxides such as MnO<sub>x</sub> polymorphs,<sup>96,111,112</sup> perovskites,<sup>113,114</sup> and spinels.<sup>27,86,115</sup> Benchmarking the electrochemical activity of single component catalysts against state-of-the-art materials, can best be done using the rotating disk electrode (RDE). Measurement variables such as scan rate, rotation rate, catalyst loading, among others should be carefully selected to create results which are comparable to a large portion of literature. A review article (co-authored by some of us) provides detailed guidelines for using RDE experiments.<sup>78</sup>

Fig. 4 shows the ORR, and OER overpotential achieved by literature catalysts at 25 μA cm<sub>oxide</sub><sup>-2</sup> in 0.1 M KOH. The specific activities of Pt/C,<sup>116</sup> and IrO<sub>2</sub><sup>117</sup> are shown in comparison. The background colouring corresponds to the voltaic efficiency of a reversible fuel cell with a flat O<sub>2</sub> catalyst surface. While Ni–Fe oxides are the most OER active catalysts,<sup>107–109</sup> they have little activity towards the ORR<sup>107</sup> and are therefore



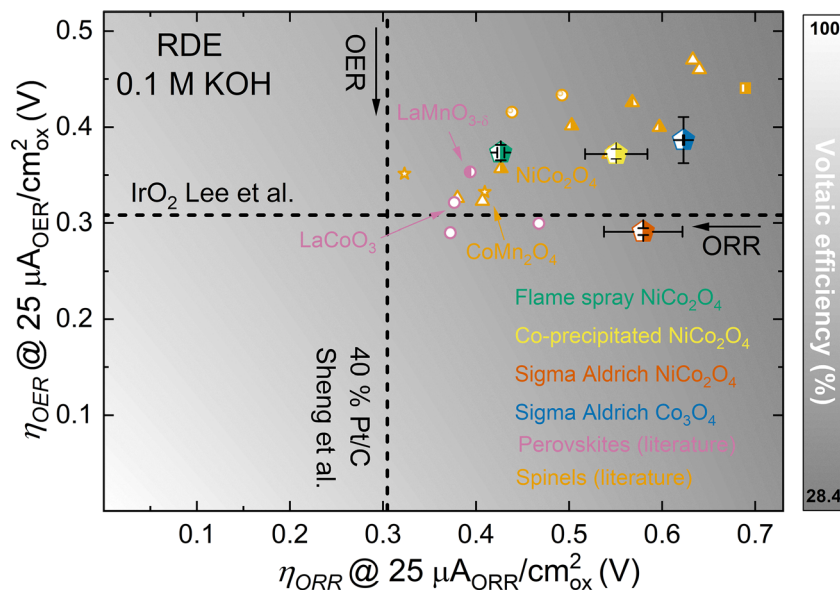


**Fig. 4** State of the art surface area normalized activity of 40% Pt/C<sup>118</sup> and activity of IrO<sub>2</sub> normalized to surface area determined from TEM particle size distribution.<sup>117</sup> All literature results have been collected in 0.1 M KOH. Colour gradient in the plot background corresponds to round trip voltaic efficiency of a reversible fuel cell with no overpotential for hydrogen catalysis and a planar catalyst surface operating at 25  $\mu$ A, 0.1 M KOH, and 1 cm<sup>2</sup>. Different symbols corresponding to data extracted from different papers investigating catalyst systems employing the following surface area normalizations:  $\blacktriangle$  data from ref. 86 normalized to nanoparticulate BET surface area;  $\blacksquare$  data from ref. 107 normalized to impedance spectroscopy electrochemical surface area;  $\blacklozenge$  48% BaSrCoFeO<sub>3</sub> + LaSrMnNiO<sub>3</sub> thin film extracted from ref. 113 and normalized to atomic force microscopy roughness;  $\bullet$  data extracted from ref. 114 and normalized to estimated surface area from SEM image analysis of drop-cast nanoparticulate thin films.  $\bullet$  data extracted from ref. 119 and normalized to nanoparticulate BET surface area;  $\star$  data extracted from ref. 120 normalized to nanoparticulate BET surface area; a thermodynamic stability analysis of each catalyst systems made with a colour code on each of the points, based on the Pourbaix diagrams.<sup>37</sup> The point is discoloured on its left or right if one its elements are unstable for the ORR (left discoloration) or OER (right discoloration).  $\blacklozenge$  coloured points correspond to original data collected in the present work, normalized to the BET surface area, and collected at a loading of 25  $\mu$ g cm<sup>-2</sup> for Flame spray NiCo<sub>2</sub>O<sub>4</sub> (green), co-precipitated NiCo<sub>2</sub>O<sub>4</sub> (yellow), Sigma Aldrich NiCo<sub>2</sub>O<sub>4</sub> (orange), and 76  $\mu$ g cm<sup>-2</sup> for Sigma Aldrich Co<sub>3</sub>O<sub>4</sub> (blue).

not plotted in Fig. 4. Each of the points in Fig. 4 is discoloured at the left or right, if at least one of its elements is thermodynamically expected to be unstable at ORR, or OER potentials respectively. Fully discoloured points correspond to materials that one or more elements are unstable at either ORR or OER potentials based on Pourbaix diagrams.<sup>37</sup> Coloured points correspond to data generated in the present work, discussed further in Section 4.1, and black and white points are literature data described in the figure caption. It is noted that glassy carbon is ORR active below 0.7 V<sub>RHE</sub>, thus having an effect on data points with an ORR overpotential bigger than 0.53 V. Therefore, throughout this text we use the current at ORR and OER potentials of 0.8 V<sub>RHE</sub> and 1.6 V<sub>RHE</sub> as performance metrics.

Fig. 4 shows that Mn-based spinel and perovskite systems,<sup>86,120</sup> as well as LaMnO<sub>3</sub>, and LaCoO<sub>3</sub><sup>114</sup> are the closest to reach the Pt/C and IrO<sub>x</sub> target.<sup>111</sup> NiCo<sub>2</sub>O<sub>4</sub> also achieves promising ORR and OER activity, with higher activity for both reactions than Co<sub>3</sub>O<sub>4</sub>, indicating the importance of Ni in catalysing both ORR and OER.<sup>27,86</sup> NiCo<sub>2</sub>O<sub>4</sub> is also a promising system since its elements –Ni and Co– are thermodynamically expected to be stable at OER potentials. In fact, NiCo<sub>2</sub>O<sub>4</sub> is the only system with demonstrated activity towards both ORR and OER,<sup>27,86</sup> which is also expected to be stable at OER relevant

potentials.<sup>37</sup> In spite of showing promise as reversible O<sub>2</sub> catalysts, its stability at ORR and OER potentials is poorly documented.

**2.1.1. Parameters controlling the activity of reversible O<sub>2</sub> catalysts.** The ORR and OER are reversed sequences of the same reaction which take place *via* four adsorption and desorption steps, as shown in (Fig. 5a), where \* denotes an active site, and its corresponding adsorbed intermediate (*i.e.* OH\* is adsorbed OH on active site \*).<sup>121,122</sup> Due to scaling relationships between the adsorbed intermediates, the reactivity towards each of the reactions is determined by the Sabatier principle.<sup>123</sup> The potential of the potential determining step is schematized in (Fig. 5b),<sup>79</sup> which corresponds to the potential at which all the reaction steps become downhill in free energy. The double volcano relationship shown in (Fig. 5b) implies that an active site with a lower overpotential towards the OER comes at the cost of ORR activity and *vice versa*.

Several experimental activity descriptors, such as *ex situ* metal center oxidation states,<sup>86,124,125</sup> and bond covalency<sup>126</sup> have been proposed to study non-precious metal oxide catalysts. However, they derive from properties of the bulk of the material rather than the properties of the oxide surface. In contrast, *ab initio* DFT calculations can model the very first monolayer of a catalyst's surface, whose properties control the



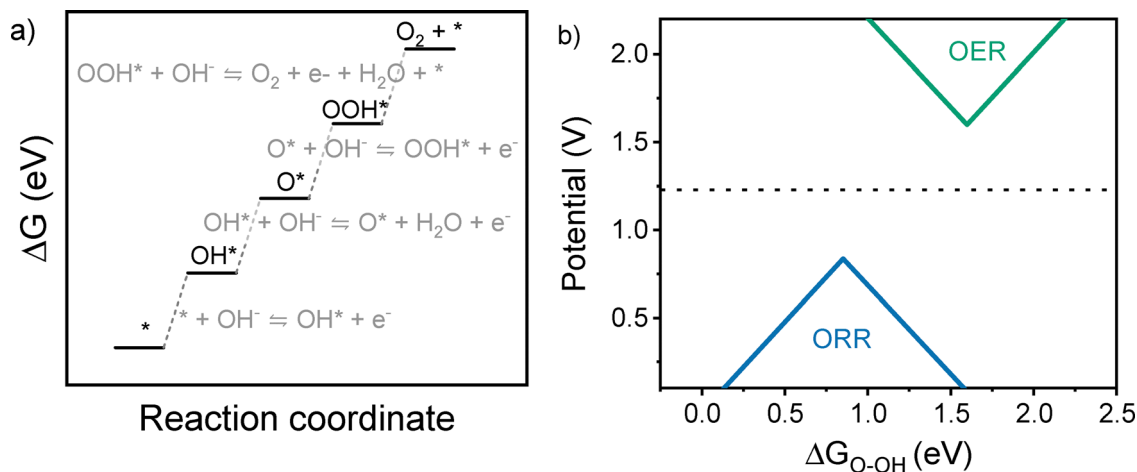


Fig. 5 (a) Schematic illustration of the free energy landscape for the OER at 0 V versus a reversible hydrogen electrode (RHE) ( $U = 0$  V), and (b) potential of the potential determining step for ORR and OER, extracted from the work of Busch *et al.*

catalysis, and can be different from the bulk of the material.<sup>79,121,127</sup> For example, the OER improvement of  $\text{NiCo}_2\text{O}_4$  with respect to  $\text{Co}_3\text{O}_4$ <sup>27,115</sup> is not explained by either oxidation state<sup>86</sup> or bond covalency arguments.<sup>126</sup> DFT on the other hand, can predict such phenomena.<sup>128,129</sup> While DFT calculations have worked well to study ORR catalysts,<sup>121,127,130</sup> under OER evolution conditions the first few atomic layers (up 5 nm from the surface) can reconstruct at anodic potentials,<sup>95,100,131</sup> compromising its predictive power for OER catalysts.<sup>117,121</sup> More generally, oxides are often challenging to describe with even the best of DFT functionals, compounding uncertainty in the calculations.<sup>132</sup> Therefore, *in situ* spectroelectrochemical studies correlating the oxidation state,<sup>133</sup> and chemical environment,<sup>100,109,134,135</sup> are most successful in describing catalyst activity. For example, Rao *et al.*<sup>133</sup> found a volcano relationship between the redox peak position of doped Ni oxides, and their activity, with a position of 1.47 V<sub>RHE</sub> as the peak of the volcano. Such studies indicate that redox transitions relate to the adsorption reaction intermediates, and the potential at which these occur relates to the catalyst's ability to bind  $\text{O}^*$  relative to  $\text{OH}^*$ . Thus, a catalyst's ability to change in oxidation state is the key to maximized OER activities.

## 2.2. Stability of reversible $\text{O}_2$ catalysts

Prevalent mechanisms by which  $\text{O}_2$  catalysts present in fuel cells and water electrolyzers can degrade are: (i) agglomeration; (ii) conductive support corrosion; (iii) detachment; and (iv) dissolution.<sup>99,136–138</sup> Agglomeration and conductive support corrosion are mostly relevant to Pt/C catalysts employed in fuel cells, which are unlikely to be applied as bifunctional catalysts due to prohibitive dissolution rates at  $\text{O}_2$  evolution potentials.<sup>94,139</sup> Detachment is also largely dependent on the specific electrode structure, and it is desirable to mitigate it during half-cell durability tests. Dissolution is considered the primary mechanism by which OER catalysts degrade in PEM electrolysis and reversible fuel cells,<sup>94,99</sup> and is likely to be the most relevant in studying reversible  $\text{O}_2$  electrodes. Dissolution can also trigger restructuring of the top surface 5 nm,<sup>100,101</sup> as

well as phase separation through redeposition processes.<sup>140,141</sup> In addition, they are highly susceptible to incorporate Fe impurities,<sup>95,142,143</sup> which increase their OER activity. Such processes are generally addressed as an activity study, but their effect on the ORR is largely misunderstood. In this manuscript, these are considered as possible degradation mechanisms, in addition to the traditional ones arising from the fuel cell and electrolysis fields.

Dissolution measurements coupling electrochemical half-cells with an inductively coupled plasma mass spectrometer (ICP-MS) are crucial to screen catalysts for electrochemical applications.<sup>143–145</sup> They can differentiate between catalysts that have a stable electrochemical signal in spite of high dissolution rates,<sup>146</sup> from losses in performance not associated with degradation mechanisms (*i.e.* backing electrode, or bubble accumulation).<sup>144,147,148</sup> Fig. 6 compiles the stability number (*i.e.* number of  $\text{O}_2$  molecules evolved per dissolved metal centre<sup>145</sup>) of different materials. Mn oxides are known to dissolve,<sup>37,96</sup> with stability numbers about 4 orders of magnitude lower than crystalline  $\text{IrO}_2$  studied in acidic electrolytes.<sup>149</sup> The few reports measuring the stability of Ni and Co based oxides indicate lower dissolution rates than Mn and Fe.<sup>143,149</sup> However, they are yet to be investigated under potentials of both ORR and OER, which is relevant since Pourbaix diagrams predict their dissolution at ORR potentials in alkaline media.<sup>37</sup>

Several researchers have theorized that lattice oxygen evolution reaction (LOER) is the predominant mechanism for  $\text{O}_2$  evolution and results in the dissolution of metal cations.<sup>100,101,131,145</sup> The LOER mechanism has been intensely debated in literature and readers are referred to a review article by Fabbri *et al.* for in-depth discussion on this topic.<sup>150</sup> However, Scott *et al.*'s data on  $\text{IrO}_x$  and  $\text{RuO}_2$  in acid suggest that LOER is a dissolution mechanism, as opposed to a catalytic reaction.<sup>137</sup> We conjecture that this may be the case for catalysts that function in base too.

Another mechanism by which catalysts could degrade is by oxidation and restructuring of the top monolayers of the catalyst's crystal structure. Oxidation processes can be probed



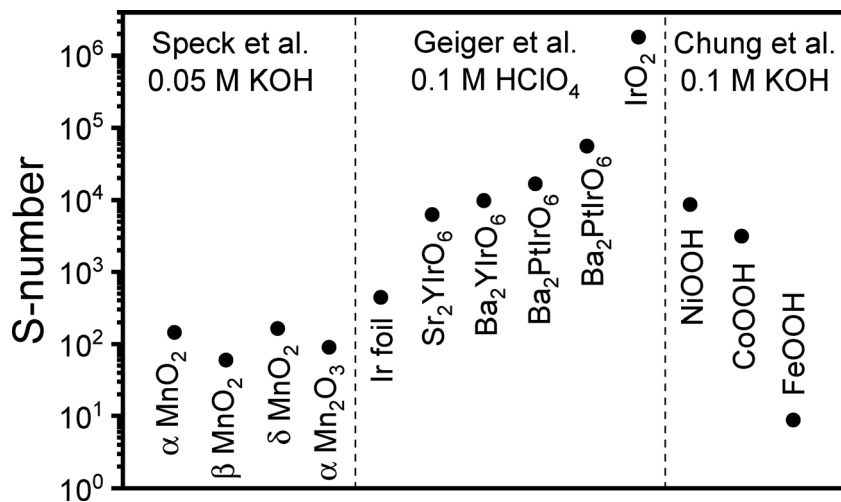


Fig. 6 Summary of *S*-numbers determined for MnO<sub>x</sub> catalysts obtained by Speck *et al.*<sup>96</sup> in alkaline media, for IrO<sub>x</sub> catalysts in acidic media determined by Geiger *et al.*,<sup>145</sup> and for electrodeposited Ni, Co, and Fe oxides determined by Chung *et al.*<sup>143</sup>

with *in situ* spectroscopic techniques such as X-ray absorption spectroscopy (XAS),<sup>109,134,151</sup> UV-vis,<sup>136,152</sup> XPS.<sup>153</sup> Correlation between such techniques and post-mortem transmission electron microscopy (TEM) indicate that oxidized catalysts result in the formation of an amorphous layer penetrating approximately the top surface 5 nm.<sup>95,101,131</sup> Researchers observe dissolution to occur during the first cycles, accompanying such amorphization, after which dissolution processes are minimised.<sup>95,100,101</sup> Changes in redox activity over time are often accompanied by such transformations. However, it is unclear to which extent they reflect changes in catalytic activity,<sup>131</sup> or merely catalytically inactive redox species in the bulk of the catalyst structure.<sup>136</sup> In addition, restructuring of the upper surface layers is often beneficial for the OER, but it is yet unclear whether it would also be beneficial towards the ORR. Similarly, small amounts of Fe impurities incorporated into nickel based oxides improve OER performance,<sup>95,142,154,155</sup> and could cause of such transformation.<sup>95,142,155,156</sup> However, the effect of such oxidation, and restructuring processes on ORR activity is unknown.

In summary, literature investigations suggest that ORR/OER activity on a particular active site follows a double volcano relationship: the higher the ORR activity, the lower its OER activity. Catalyst OER activity correlates with its ability to change in oxidation state, which are a fingerprint of the adsorption of reaction intermediates.<sup>133</sup> Co-Mn perovskite and spinel oxide catalysts are identified as the most active bifunctional catalysts for both ORR and OER, but their stability across the ORR/OER potential window has not been measured.<sup>86,107,111,114,120</sup> During operation in an electrochemical device, dissolution is the most likely mechanism by which oxide catalysts are expected to degrade. For some catalysts, it has been proposed that oxidation and amorphization of the upper surface monolayers halts dissolution and is the key to increased activity.<sup>100,101,131</sup> However, the effect of such a process on the ORR activity is unknown. To the best of our

knowledge, the lack of information about degradation mechanisms for the ORR/OER is a major gap in metal-air battery literature. Therefore, it is of paramount importance to develop a single methodology that assesses all the different degradation mechanisms that can possibly occur within a catalyst system. Therefore, we use original data in this perspective as a representative case study to exemplify a methodology that can be applied to interrogate multiple degradation pathways in a single system: NiCo<sub>2</sub>O<sub>4</sub>.

NiCo<sub>2</sub>O<sub>4</sub> catalysts have been demonstrated to satisfy each of the following criteria (i) to show some activity towards for ORR (ii) activity for OER, and (iii) thermodynamically stable over the pH > 13 and at potentials anodic of 1.23 V<sub>RHE</sub> and potential range required (0.6 to 1.8 V RHE and pH > 13). Although short term tests suggest that NiCo<sub>2</sub>O<sub>4</sub> is stable in catalysing the OER,<sup>115,156,157</sup> we anticipate that there might be some underlying degradation which would be difficult to detect by short term electrochemical tests. Tests of NiCo<sub>2</sub>O<sub>4</sub> in gas diffusion electrodes for both ORR and OER suggest that it deactivates faster for ORR than the OER.<sup>29,150</sup> However, in gas diffusion electrodes it is challenging to distinguish effects due to flooding of the electrode and ORR deactivation. Therefore, we use this catalyst system to inquire about the underlying degradation mechanisms occurring at potentials of both ORR and OER.

### 3. Results and discussion

In this contribution, the activity of NiCo<sub>2</sub>O<sub>4</sub> is studied as a function of its crystal structure, by combining RDE and physical characterization techniques. In addition, we used an RDE cell to enable accurate measurement of dissolution processes and couple it with both post-mortem characterization techniques, and *in situ* X-ray absorption spectroscopy. This array of techniques is used to study spinel NiCo<sub>2</sub>O<sub>4</sub>, namely the



deterioration of its ORR activity when subjected to both ORR and OER potentials.

### 3.1. Activity of reversible NiCo<sub>2</sub>O<sub>4</sub> catalysts

Prior to analysing the activity of Ni–Co oxides, the activity of Pt/C and IrO<sub>x</sub> was benchmarked, as shown in Fig. S2. The activity of oxides investigated in the present work was previously shown in Fig. 4 using the overpotential at a particular current as performance metric. However, as shown in Fig. S3, it is preferable to use the current at 0.8 V<sub>RHE</sub> as a measure of intrinsic ORR activity, due to the activity of glassy carbon. The current at 1.6 V<sub>RHE</sub> is used as OER activity metric, a potential which minimizes mass transport overpotentials while avoiding contribution from redox activity. Fig. 7 shows the electrochemical activity of Ni–Co oxides investigated in the present work, normalized to the BET surface area values shown in Table S1. XRD results shown in Fig. S4 indicate that Sigma Aldrich NiCo<sub>2</sub>O<sub>4</sub> has a rock salt crystal structure, whereas flame spray NiCo<sub>2</sub>O<sub>4</sub>, co-precipitated NiCo<sub>2</sub>O<sub>4</sub>, and Sigma Aldrich Co<sub>3</sub>O<sub>4</sub> display spinel structures. We find that rock salt NiCo<sub>2</sub>O<sub>4</sub> is essentially inactive towards the ORR, while having higher activity towards the OER. The spinel structure therefore reaches a compromise between ORR and OER activity, as shown in Fig. 4. Spinel NiCo<sub>2</sub>O<sub>4</sub> is also found to be more active than spinel Co<sub>3</sub>O<sub>4</sub> for both ORR and OER, in good agreement with previous studies.<sup>27,115</sup>

EELS structure maps shown in Fig. 8 further elucidate the differences in activity between the different catalysts. They suggest that a significant amount of Ni rich rock salt impurities is present at the surface of co-precipitated NiCo<sub>2</sub>O<sub>4</sub>, which were not observed by XRD. Rock salt impurities in the flame spray NiCo<sub>2</sub>O<sub>4</sub> are found to be within the particle's core. The surface of the flame spray synthesised catalyst is dominated by the spinel phase. Since the catalytic activity would be controlled by the surface, we conjecture that the spinel phase has a higher ORR specific activity, hence explaining the performance of the flame spray catalyst. We propose that if we were able to minimise the amount of rock salt impurities when synthesizing NiCo<sub>2</sub>O<sub>4</sub> catalysts we could maximise the ORR activity.

Consistent with our earlier analyses on NiO<sub>x</sub>,<sup>133</sup> we assume that the redox peak positions are due to transitions between O<sub>2</sub> evolution intermediates, OH\* to O\*. The full redox reaction can be expressed as M<sup>x</sup>OOH + OH<sup>-</sup> ↔ M<sup>x+1</sup>OO + e<sup>-</sup> + H<sub>2</sub>O<sup>129,133</sup> where M<sup>x</sup> denotes initial Co<sup>3+</sup> or Ni<sup>3+</sup> states in octahedral sites or Co<sup>2+</sup> in tetrahedral sites.<sup>86</sup> Thus, cathodic shifts in redox peaks position could be caused by stronger binding of O\* relative to OH\*, *i.e.* a lower ΔG<sub>O-OH</sub> (Fig. 5b). Such correlation is shown in Fig. S6, and is based on redox peak positions shown in Fig. S5, where cathodic shifts in redox activity result in increased OER activity. Trends in OER activity point towards Ni–Co oxides being located at the weak O\* binding side of the volcano. Trends for the ORR seem to point towards maximized activities at redox peak positions ~1.4 V<sub>RHE</sub> but more points would be required for conclusive evidence. These results indicate that indeed redox activity controls OER, and possibly ORR activity.

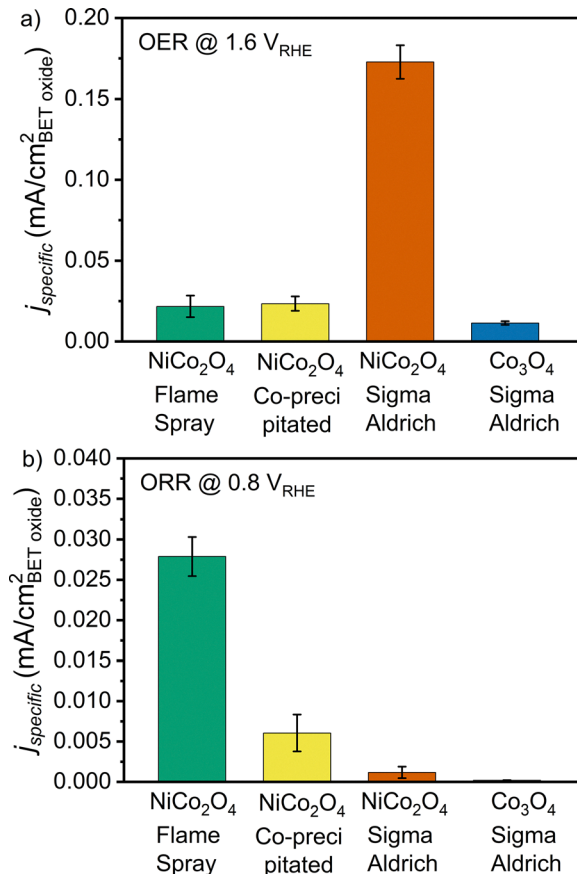


Fig. 7 (a) Electrochemical specific activity towards the OER at 1.6 V<sub>RHE</sub>, and (b) ORR at 0.8 V<sub>RHE</sub> (blue), of oxides investigated in the present work, using BET specific surface areas determined for co-precipitated NiCo<sub>2</sub>O<sub>4</sub> (107 m<sup>2</sup> g<sup>-1</sup>), Sigma Aldrich NiCo<sub>2</sub>O<sub>4</sub> (11 m<sup>2</sup> g<sup>-1</sup>), Sigma Aldrich Co<sub>3</sub>O<sub>4</sub> (46 m<sup>2</sup> g<sup>-1</sup>), and Flame sprayed NiCo<sub>2</sub>O<sub>4</sub> (74 m<sup>2</sup> g<sup>-1</sup>). All results obtained in 0.1 M KOH electrolyte at a scan rate of 10 mV s<sup>-1</sup>, rotation speed of 1600 RPM, loading of 25 μg cm<sup>-2</sup>, under O<sub>2</sub> bubbling at 150 mL min<sup>-1</sup>.

Suntivich *et al.*<sup>105</sup> argue that the activity of a non-PGM catalyst is satisfactory if the extrapolated activity of a 100 μm thick catalyst layer<sup>106</sup> matches the activity of a Pt/C electrode at a loading of 0.4 mg<sub>Pt</sub> cm<sup>-2</sup>. Extrapolations are based on mass activity, catalyst density and an assumption of 50% catalyst layer porosity. Such calculations yield projected ORR geometric activities of ~250 mA cm<sup>-2</sup>, and ~135 mA cm<sup>-2</sup>, respectively, for Pt/C and Co-precipitated NiCo<sub>2</sub>O<sub>4</sub> electrodes at loadings of 0.4 mg<sub>Pt</sub> cm<sup>-2</sup>, and ~30 mg<sub>NiCo<sub>2</sub>O<sub>4</sub></sub> cm<sup>-2</sup> at 0.8 V<sub>RHE</sub>. For the flame spray NiCo<sub>2</sub>O<sub>4</sub> synthesized at 15 L<sub>O<sub>2</sub></sub> min<sup>-1</sup>, an extrapolated activity of ~630 mA cm<sup>-2</sup> is obtained at 30 mg<sub>NiCo<sub>2</sub>O<sub>4</sub></sub> cm<sup>-2</sup>, and 0.8 V<sub>RHE</sub>, thus having the potential to fulfil the activity targets set by Pt/C catalysts. It is noted that deviations from the values provided in the original paper for Pt/C<sup>105</sup> are due to mass-transport-corrections not being employed in the present work, due to undefined diffusion limiting currents obtained for oxides.

### 3.2. Potential dependent electrochemical stability of NiCo<sub>2</sub>O<sub>4</sub>

Fig. 9 shows electrochemical activity of co-precipitated NiCo<sub>2</sub>O<sub>4</sub> for the ORR and OER, before and after cycling the potential



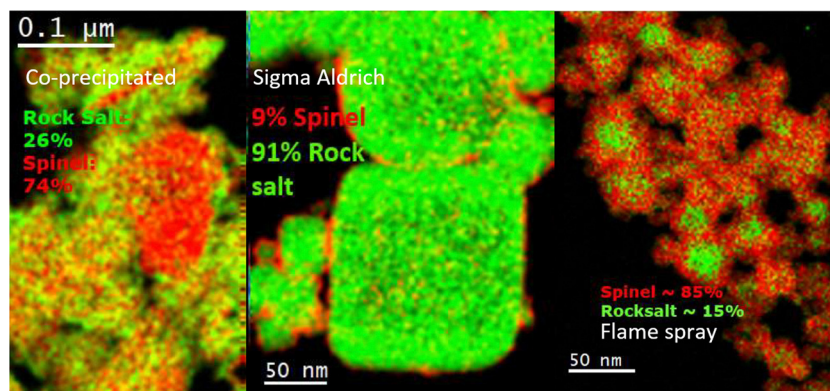


Fig. 8 Phase maps obtained by processing of electron energy loss spectra collected for Co-precipitated  $\text{NiCo}_2\text{O}_4$ , Sigma Aldrich  $\text{NiCo}_2\text{O}_4$  and Flame sprayed  $\text{NiCo}_2\text{O}_4$ .



Fig. 9 Geometric electrochemical activity of co-precipitated  $\text{NiCo}_2\text{O}_4$  before (full line), and after (dashed line) cycling for 1 h between  $0.6 V_{\text{RHE}}$  and  $1.7 V_{\text{RHE}}$  at  $500 \text{ mV s}^{-1}$ . Results collected in  $0.1 \text{ M KOH}$ ,  $\text{O}_2$  bubbling at  $150 \text{ mL min}^{-1}$ , at  $1600 \text{ RPM}$ ,  $10 \text{ mV s}^{-1}$ , and a loading of  $76 \mu\text{g}_{\text{NiCo}_2\text{O}_4} \text{ cm}^{-2}$ .

between  $0.6 V_{\text{RHE}}$  and  $1.7 V_{\text{RHE}}$  for 1 hour at  $500 \text{ mV s}^{-1}$ . While the OER activity is essentially unchanged,  $\text{NiCo}_2\text{O}_4$  becomes practically inactive towards the ORR after 1 hour of cycling. The change in values for different test repeats is shown in Fig. S7. At the same time, an additional redox peak is measured at around  $1.3 V_{\text{RHE}}$  after electrochemical cycling. Such an observation could be an indication of a stronger  $\text{O}^*$  binding relative to  $\text{*OH}$ . This shift could occur due to surface composition changes (*i.e.* caused by dissolution), crystal structure changes at the upper surface layers and/or irreversible changes in oxidation state.

Prior to elucidating which mechanism causes ORR degradation, we aim to understand which potential windows are triggering such phenomena. To do so, apply electrochemical accelerated stress tests with three different potential windows: (i)  $0.6\text{--}1.7 V_{\text{RHE}}$ ; (ii)  $0.6\text{--}1.5 V_{\text{RHE}}$ ; and  $0.6\text{--}1 V_{\text{RHE}}$ . This experimental matrix allows us to determine if ORR degradation occurs at potentials of redox activity, or during OER. Fig. 10 shows that ORR deactivation occurs during exposure to redox and OER activity potentials. When  $\text{NiCo}_2\text{O}_4$  is cycled between

$0.6 V_{\text{RHE}}$  and  $1 V_{\text{RHE}}$  over 1 hour, there is minimal ORR degradation. When the anodic potential window limit is increased, ORR degradation is observed, thus concluding that it takes place at potentials anodic of  $1\text{--}1.2 V_{\text{RHE}}$ .

### 3.3. Degradation mechanisms of $\text{NiCo}_2\text{O}_4$ reversible $\text{O}_2$ catalysts

Based on available literature the ORR degradation of spinel  $\text{NiCo}_2\text{O}_4$  upon polarization anodic of  $1\text{--}1.2 V_{\text{RHE}}$  could be due to: (i) composition changes due to dissolution;<sup>37,143,155</sup> (ii) crystal structure changes at the top surface atomic layers;<sup>101,131</sup> or (iii) Fe impurities in the electrolyte.<sup>95,155</sup> Fig. 11 shows the ICP-MS results of probing the electrolyte for Ni and Co after cell assembly, where the  $\text{NiCo}_2\text{O}_4$  catalysed RDE tip was immersed in the electrolyte, and after 1 hour of AST. 1 hour of cycling between  $0.6\text{--}1.7 V_{\text{RHE}}$  results in no more than 0.3 wt% of Ni and 0.2 wt% of Co dissolution. By subtracting the cell baseline, we determine an average dissolution of about 0.1 wt% Ni and Co which corresponds to about 2% and 4% of a BET monolayer of Co and Ni respectively. We calculate the dissolution rate in BET monolayers from crystallographic considerations of atomic Co coverage for (110) and (100) surfaces on spinel  $\text{Co}_3\text{O}_4$  from the work of Zasada *et al.* as described in the SI.<sup>158</sup> In the next paragraphs, we estimate the surface composition changes that would result from the dissolution process and compare it with surface composition changes measured by XPS.

Fig. S8 shows the XPS spectra measured for co-precipitated  $\text{NiCo}_2\text{O}_4$  catalyst layers after immersion in the  $0.1 \text{ M KOH}$  electrolyte labelled initial, and after undergoing an AST, labelled aged. In such measurements, we observed increases in Co:Ni surface compositions from 1.35 to 1.6. The observed increase in Co:Ni ratio is not very significant and cannot explain the drastic decrease in ORR activity. Additionally, the dissolution of Ni is only 4% of a monolayer which does not explain the change in ORR activity. Further calculations of extrapolated dissolution rates associated with the composition changes observed by XPS are referred to the SI.

Other research groups measure OER to induce the amorphization of the top surface 5 nm, which we consider as a possible





**Fig. 10** Geometric electrochemical activity of co-precipitated  $\text{NiCo}_2\text{O}_4$  before (full line), and after (dashed line) cycling for 1 h between  $0.6 V_{\text{RHE}}$  and three different anodic limits of  $1.7 V_{\text{RHE}}$  (blue),  $1.5 V_{\text{RHE}}$ , and  $1 V_{\text{RHE}}$  at  $500 \text{ mV s}^{-1}$ , as described in the figure labels. Results collected in  $0.1 \text{ M KOH}$ ,  $\text{O}_2$  bubbling at  $150 \text{ mL min}^{-1}$ , at  $1600 \text{ RPM}$ ,  $10 \text{ mV s}^{-1}$ , and a loading of  $76 \mu\text{g}_{\text{NiCo}_2\text{O}_4} \text{ cm}^{-2}$ .

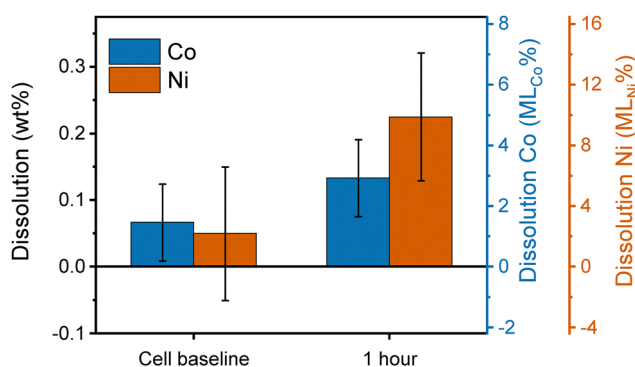


**Fig. 11** ICP-MS results after acidification of  $150 \text{ mL}$  of the  $0.1 \text{ M KOH}$  electrolyte employed in rotating disk electrode configuration to study co-precipitated  $\text{NiCo}_2\text{O}_4$ . Cell baseline taken after assembling the RDE configuration, and 1 hour is taken after cycling between  $0.6\text{--}1.7 V_{\text{RHE}}$  for 1 hour at  $500 \text{ mV s}^{-1}$  without any RDE rotation and employing an anion exchange membrane to separate the counter electrode from the working electrode at a loading of  $76 \mu\text{g}_{\text{NiCo}_2\text{O}_4} \text{ cm}^{-2}$ . Calculations of Ni and Co dissolved monolayers are based on  $0.076 \text{ Co atoms per } \text{\AA}^2$  derived from the work of Zasada *et al.*,<sup>158</sup> and the BET surface area of Co-precipitated  $\text{NiCo}_2\text{O}_4$  ( $107 \text{ m}^2 \text{ g}^{-1}$ ). Dissolved Ni in %ML is the ratio between dissolved Ni atoms and total available surface Ni atoms in the RDE catalyst layer as described in the SI.

degradation mechanism for  $\text{NiCo}_2\text{O}_4$ .<sup>100,131,151</sup> As shown in Fig. S9, post-mortem TEM shows that an amorphous surface oxyhydroxide layer is not formed. Herein, we avoid

misinterpretation of the results due to carbon contamination, which can form similar features, as shown in Fig. S10. We also consider the possibility that such a layer forms exclusively in the presence of Fe impurities. Post-mortem TEM after accelerated stress tests in  $0.1 \text{ M KOH}$  poisoned with 50 PPB of Fe impurities discards such a hypothesis, as shown in Fig. S13.

Pourbaix diagrams would suggest that Ni and Co dissolution should take place cathodic of  $0.9 V_{\text{RHE}}$  at pH 13<sup>37</sup>. However, our electrochemical tests on coprecipitated  $\text{NiCo}_2\text{O}_4$  suggest that degradation is triggered by potentials anodic of  $1 V_{\text{RHE}}$ . Minimal compositional changes due to dissolution are detected with ICP-MS (see Fig. 11) and post-mortem XPS (see Fig. S8), indicating that dissolution is not the cause of ORR degradation (see Fig. 9). These findings are consistent with post-mortem TEM which shows no evidence of structural rearrangement of  $\text{NiCo}_2\text{O}_4$  in the near surface region prone to structural amorphization at the top monolayers (Fig. S9). In contrast to observations on  $\text{AlCoFeO}_x$ <sup>101</sup> and  $\text{Ba}_{0.5}\text{Sr}_{0.5}\text{Co}_{0.8}\text{Fe}_{0.2}\text{O}_3$ ,<sup>100</sup> we do not observe indications of dissolution or amorphization of the outermost few nm of Co-precipitated  $\text{NiCo}_2\text{O}_4$ . However, both findings indicate that dissolution can trigger structural changes of the top few nm, and that its absence results in a preserved crystal structure.

Fig. 12 shows the X-ray absorption near edge structure (XANES) portion of the collected *in situ* XAS spectra. We measure the oxidation state of Co-precipitated  $\text{NiCo}_2\text{O}_4$  at different potentials, stepping the potential in the anodic





Fig. 12 *In situ* XANES spectra recorded for co-precipitated  $\text{NiCo}_2\text{O}_4$  starting at  $0.6 V_{\text{RHE}}$ , progressively scanning anodically up to  $1.7 V_{\text{RHE}}$ , and then perform a last measurement at  $0.6 V_{\text{RHE}}$ . The latter which is labelled as  $0.6 V_a$ . (a) Ni edge, and (b) Co edge. Measurements taken at a loading of  $76 \mu\text{gNiCo}_2\text{O}_4$  in  $0.05 \text{ M KOH}$ .

direction, starting at  $0.6 V_{\text{RHE}}$  up to  $1.7 V_{\text{RHE}}$ . We then polarize the electrode back to  $0.6 V_{\text{RHE}}$ , to measure changes in oxidation state after polarization to anodic potentials. Interestingly, the oxidation states of both Ni and Co increase as the potential increases and, while this oxidation is reversible for Ni centres, Co displays irreversible oxidation upon OER polarization. After OER polarization, the average oxidation state of Co at  $0.6 V_{\text{RHE}}$  increases from  $\text{Co}^{2.2+}$  to  $\text{Co}^{2.3+}$ . Assuming that all the changes in oxidation state occur within the first top monolayer, the oxidation state change of Co atoms can be calculated as per the calculations section of the SI. Assuming that all Co atoms have an initial oxidation state of  $\text{Co}^{2.2+}$ , an increase of 0.1 in oxidation state results in the surface Co atoms having an oxidation state of  $\text{Co}^{3.1+}$  at  $0.6 V_{\text{RHE}}$ . Such a number could be accounted for by a single redox transition which is consistent with the fact that only one redox peak is observed for  $\text{NiCo}_2\text{O}_4$ . As shown in Fig. S13, Ni mostly occupies octahedral sites due to the missing peak at  $3 \text{ \AA}$  on the Ni K edge spectra.<sup>86</sup> Thus, Co occupies both tetrahedral  $\text{Co}^{2+}$  sites, and octahedral  $\text{Co}^{3+}$  sites, which means that irreversible oxidation could happen preferentially at one of these sites, and to a higher valence than the calculated  $\text{Co}^{3.1+}$ . This observation indicates that catalysing the ORR requires Co to remain at a low oxidation state, and promoting reversible oxidation processes after OER is key for  $\text{NiCo}_2\text{O}_4$  to retain its ORR activity.

It is noted that the edge position shift is smaller than the energy resolution of the X-ray scan. This can be attributed to the low surface area to volume ratio of the particles ( $\sim 40 \text{ nm}$  in size), considering that the XAS are bulk sensitive, while the electrochemical reactions occur only on the surface. Nonetheless, such an effect could explain the ORR degradation observed in Fig. 9. Extended X-ray fine structure (EXAFS) results were also taken, as shown in Fig. S15–18. Shortening bonding distances are observed as the potential is increased, which are not fully recovered after OER polarization. Such irreversible trends were also small for the Co edge and neglectable for Ni, in good agreement with XANES results.

Even though dissolution and structural changes were not observed, irreversible changes in Co oxidation were measured by *in situ* XAS. While it could be possible that such results are due to poor quality of the data or fits due to the large particle size, extensive characterization was done to rule out prevalent degradation mechanisms. The irreversible oxidation of Co centers could explain the appearance of an additional redox peak at  $\sim 1.3 V_{\text{RHE}}$  after anodic polarization. This redox peak could correspond to Co active sites with higher oxidation state, and stronger  $\text{O}^*$  binding energy than the initial oxidation state. Such changes in oxidation state could render Co sites inactive towards the ORR. The OER likely predominates at Ni sites, thus why OER activity is unaffected by the irreversible oxidation of Co.

## 4. Conclusion

In this paper, we reviewed the main strategies to bring zinc–air batteries to technological fruition. The stability of the main components is the limiting factor, and especially that of the air–electrode. Literature indicates that Mn based oxides are the most active materials available, but their dissolution rates at OER potentials are prohibitive for industrial application. We identify  $\text{NiCo}_2\text{O}_4$  as a promising system with activity comparable to the best catalysts in literature. Furthermore, we developed a novel methodology to screen reversible  $\text{O}_2$  catalyst activity, which is applicable to a broader set of catalyst materials.

In the present work, we find that both structure and composition are important factors controlling the activity of  $\text{NiCo}_2\text{O}_4$ .  $\text{Co}_3\text{O}_4$  is inactive towards the ORR, and Ni in  $\text{NiCo}_2\text{O}_4$  improves both ORR and OER activity with respect to its mono-metallic oxide counterpart. Considering a double volcano relationship between ORR and OER, such finding indicates that ORR and OER is catalysed on different active sites. A study of model materials has also identified that rock salt  $\text{NiCo}_2\text{O}_4$  is inactive towards the ORR, while being more OER active than



spinel  $\text{NiCo}_2\text{O}_4$ . It is concluded that future research efforts should comprise of synthesizing phase pure spinel  $\text{NiCo}_2\text{O}_4$  electrocatalysts while avoiding the presence of rock salt impurities. In addition, a  $\text{NiCo}_2\text{O}_4$  synthesized by flame spray pyrolysis achieved promising mass activities,<sup>106</sup> and can be a good candidate to be applied in reversible zinc–air batteries.

The stability of spinel  $\text{NiCo}_2\text{O}_4$  as ORR and OER catalyst was assessed with the RDE. It is found that  $\text{NiCo}_2\text{O}_4$  is stable in catalysing the ORR and OER separately, but unstable towards the ORR when exposed to both ORR and OER potential windows. Both redox and OER activity occurring at potentials anodic of  $1 \text{ V}_{\text{RHE}}$  trigger ORR degradation. Dissolution of either Ni or Co did not account for such severe degradation, with a lower detection limit of about 4% of a Ni monolayer, and 2% of a Co monolayer. At the same time, no evidence was found suggesting the formation of an amorphous oxyhydroxide penetrating the upper few surface layers of the catalyst structure, a phenomenon that is usually associated with dissolution. Furthermore, we suggest that future studies address possible losses in electrical conductivities in the catalyst, which would be more pronounced in air electrodes using higher loadings. It is proposed that  $\text{NiCo}_2\text{O}_4$  can be used as a comparison baseline material when that could potentially retain its electrical conductivity due to suppressing amorphization at the surface.

*In situ* XAS experiments were performed to understand degradation processes occurring at potentials anodic of  $1 \text{ V}_{\text{RHE}}$  which cause ORR degradation. It is found that the oxidation state of Co in  $\text{NiCo}_2\text{O}_4$  at  $0.6 \text{ V}_{\text{RHE}}$  increases irreversibly after exposure to anodic potentials, whereas the oxidation state of Ni is fully recovered. Such sites would have a higher oxidation state and stronger  $\text{O}^*$  binding energy, which is reflected in the appearance of an additional redox peak at more cathodic potentials. Assuming that ORR and OER are catalyzed on different active sites, it is likely that ORR takes place on Co sites which become inactive when oxidized. At present, this is the only data set shedding light onto the degradation of  $\text{NiCo}_2\text{O}_4$  as a reversible  $\text{O}_2$  catalyst. At the same time, it is one of the few papers using *in situ* spectroelectrochemical techniques to probe degradation. The insight gained from such experiments points towards coupling DFT and *in situ* spectroelectrochemical techniques as a promising strategy to increase the lifetime of reversible  $\text{O}_2$  catalysts.

#### 4.1 Challenges and perspective

In this paper, we reviewed the main strategies to bring zinc–air batteries to technological fruition. The stability of the main components is the limiting factor, and especially that of the air–electrode. Zinc–air batteries have a value proposition of cheap and recyclable active species, and are likely to become competitive with all vanadium flow batteries if durability issues are solved. Due to their inherently lower round trip efficiency, Zn–air batteries would also need to leverage short periods of cheap or free electricity to become viable. Thus, it is essential to focus on the long-term durability and lowering the cost of materials for zinc–air redox flow batteries. This perspective highlights the need for prioritizing the following research

topics in developing integration strategies for metal–air batteries:

**4.1.1. Deepen understanding of challenges and benefits of using Zn slurry configuration.** The most promising strategy to scale up zinc–air batteries includes the Zinc-slurry configuration, since capacity is not limited by electrode size.<sup>25,26</sup> Such a configuration could also mitigate some of the issues related to dendrite formation during charge cycles, and passivation during discharge. Pressing issues to research include understanding how to formulate a Zinc-slurry, to minimize pumping losses, and maximize zinc utilization. In this configuration, shunt currents could become an issue due to incorporation of electrically conductive material to the flowing electrolyte. Even though the Zn electrode was not extensively covered in this perspective, we argued that achieving a stable chemistry at the metal electrode is key to enable rechargeable Zn–air batteries.

**4.1.2. Design and assess the need for stable anion exchange membranes.** Anion exchange membranes have the potential to minimize the ohmic drop, increase the maximum operable current density, and thus decrease stack size. However, it is unclear if this could result in a decrease in stack cost, for which a cost trade-off between membrane implementation and stack size reduction should be studied with techno-economic analyses. This type of analysis should be carried out at the point when stable AEM chemistries have been found. It would also be important for zinc–air batteries to study AEM products with the necessary mechanical properties to withstand the abrasive nature of a flowing slurry.

**4.1.3. Develop a stable electrode that can catalyse both ORR and OER.** Because of limitations in catalyst stability, the bi-electrode configuration is at present the best solution to implement flow batteries using  $\text{O}_2$  as an active species.<sup>19,63,96</sup> However, using a single air–electrode to catalyse both ORR and OER is the key to reduce capital cost of installed battery capacity.<sup>19</sup> Some of the most promising high surface area catalysts developed might appear stable in short-term measurements, but not in the long-term due to dissolution processes.<sup>28,63,88,94</sup> Within this topic, we propose the following order by which researchers should prioritize scientific discoveries:

**4.1.3.1. Identification of ORR and OER catalytically active materials.** Finding a single material that can catalyse both ORR and OER is the most promising strategy to develop reversible  $\text{O}_2$  electrodes, and a requirement to be met before investigations on electrochemical stability. Mixing two catalyst composition is a possible strategy to overcome scaling relationships, but has the drawback of likely introducing more elements that are likely to be thermodynamically unstable (see Fig. 4). However, this is a possible strategy provided that the ORR active catalyst is stable at OER potentials, and the OER catalyst is stable at ORR potentials. We stress that several materials have been found that could be deemed sufficiently active, but their stability is yet to be determined. A review of state-of-the-art catalysts in literature (see Fig. 4) indicates that Mn–Co mixed oxides are the most ORR/OER active materials available. Along  $\text{NiCo}_2\text{O}_4$ , these are good candidates as



materials for further improvements in activity, and stability investigations.

**4.1.3.2. Understanding the electrochemical degradation mechanisms taking place during ORR and OER.** Future research efforts to design reversible O<sub>2</sub> catalysts should focus on screening catalysts using experimental methods to measure dissolution. Down selected materials that are not prone to dissolution, but still degrade (such as NiCo<sub>2</sub>O<sub>4</sub>), should be studied for possible changes in surface structure, and/or oxidation state changes. The techniques employed in the present work, such as post-mortem TEM, and *in situ* XAS are good frameworks to study degradation caused by amorphization and oxidation of the catalyst.<sup>100,151</sup> Electrochemical cycling profiles similar to those employed in this work can also be coupled with other *in situ* techniques such as UV-vis or Raman spectroscopy. Among these, UV-vis shows promise to probe redox processes associated with the adsorption of reaction intermediates.<sup>133,136,152</sup> Its rather small spectra collection times could enable convenient time resolutions for degradation studies attempting to develop a deeper understanding of redox activity changes over time. Correlating such *in situ* measurements with insight from DFT is also a potential strategy to study catalyst stability. Calculations of O\* binding energies for different coverages of reactive intermediates on NiCo<sub>2</sub>O<sub>4</sub> facets<sup>128</sup> could be related to the double volcano relationships described by Busch *et al.*<sup>79</sup> Such a study could then lay the groundwork for introducing new dopants or other compositions which retard or inhibit irreversible oxidation processes.

**4.1.3.3. Development of gas diffusion layers and conductive supports that are stable at OER potentials.** Finding stable materials that can be implemented at the gas diffusion layer of the air electrode, as well as conductive additive for the catalyst layer is important once a stable catalyst is found. Future scientific efforts should comprise of evaluating the stability of both catalyst and conductive support components separately. Carbon is a typical material and increasing its stability at OER potentials could be particularly fruitful in developing reversible electrodes for metal–air batteries. In this research strategy, we suggest that byproducts of carbon degradation such as CO or carbonates are analyzed with gas analysis techniques such as in-line mass spectroscopy,<sup>97</sup> or ion chromatography,<sup>98</sup> respectively.<sup>159,160</sup> Such techniques would allow studying the degradation mechanisms without relying solely on the electrochemical current as a screening tool for different catalyst layer formulations. Metallic Ni powder is a possible catalyst support but other conductive oxides or boron doped diamond are also promising and subject of little investigations.

**4.1.3.4. Fabrication and electrochemical testing of gas diffusion electrodes in half-cell configuration.** Methods to test the effectiveness of catalysts at the highly alkaline environment at pH > 14 require half-cell tests in gas diffusion electrode configuration. These conditions could accelerate catalyst dissolution, and passivation of the gas diffusion layer materials. Therefore, half-cell GDE dissolution measurements at higher molarity

could be important to demonstrate feasibility, and optimization of materials integration in a zinc–air battery prototype. We anticipate that dissolution may be hindered at high catalyst loadings due to Nernstian stabilisation effects.<sup>99,161,162</sup>

**4.1.3.5. Integrate components in single cell zinc–air battery prototype test bench.** Single cell measurements represent significant technological development, and the last step to demonstrate optimized conditions before field trials and upscaled solutions. However, we take the view that zinc–air battery technologies are too early in the research cycle for widespread implementation of demonstration-scale experimental procedures involving single-cell tests. At present, it should be more fruitful to develop lab scale procedures to understand the fundamental aspects of Zn electrodeposition, and electrocatalyst activity and durability outlined in this manuscript. We suggest that Zn–air batteries are a promising technology for large scale energy storage. However, considerable advancements need to be carried out in studying the durability of their main components; especially the air–electrode catalyst whose literature is under represented. The progress carried out in this paper sets a foundation to methodologies and framework that can be used to further screen catalysts for Zn–air batteries.

## Conflicts of interest

There are no conflicts to declare.

## Data availability

Data for this article, including CIF files for Co<sub>3</sub>O<sub>4</sub> is available at <https://www.crystallography.net/cod>.

Further data supporting this article have been included as part of the supplementary information (SI). Supplementary information is available. DOI: <https://doi.org/10.1039/d5ey00236b>.

## Acknowledgements

This project has received funding from the European Union's Horizon 2020 research and innovation programme under Grant Agreement no. 765289 (FlowCamp) and 866402 (NitroScission). The authors would like to thank Diamond Light Source for beamtime (experiment no. SP27861), and the staff of beamline B18 for assistance with testing and data collection.

## References

- 1 IEA, CO<sub>2</sub> Emissions from Fuel Combustion: Overview, IEA, Paris, 2020, <https://www.iea.org/reports/co2-emissions-from-fuel-combustion-overview>.
- 2 B. Looney, *Statistical Review of World Energy*, 69th edn, 2020, vol. 69, p. 66 [Online]. Available: <https://www.bp.com/content/dam/bp/business-sites/en/global/corporate/pdfs/energy-economics/statistical-review/bp-stats-review-2020-full-report.pdf>.



- 3 D. M. R. Abbas, A. Akhil, G. Huff, A. B. Currier, B. C. Kaun, W. D. G. Stella, B. Chen, A. L. Cotter and D. T. Bradshaw, DOE/EPRI 2013 Electricity Storage Handbook in Collaboration with NRECA, 2013, [Online]. Available: <https://www.sandia.gov/ess/publications/SAND2013-5131.pdf>.
- 4 B. Chalamala, DOE OE Global Energy Storage Database, Sandia National Laboratories. [Online]. Available: <https://www.sandia.gov/ess-ssl/global-energy-storage-database/>.
- 5 U. Energy Information Administration, Battery Storage in the United States: An Update on Market Trends, 2021. [Online]. Available: <https://www.eia.gov>.
- 6 Database of the European energy storage technologies and facilities. [Online]. Available: <https://data.europa.eu/data/datasets/database-of-the-european-energy-storage-technologies-and-facilities?locale=en>.
- 7 K. Mongird, *et al.*, *Energy Storage Technology and Cost Characterization Report*, 2019.
- 8 N. Nasajpour-Esfahani, H. Garmestani, M. Bagheritabar, D. Jasim, D. Toghraie, S. Dadkhah and H. Firozeh, Comprehensive review of lithium-ion battery materials and development challenges, *Renewable Sustainable Energy Rev.*, 2024, **203**, 114783, DOI: [10.1016/j.rser.2024.114783](https://doi.org/10.1016/j.rser.2024.114783).
- 9 T. Bowen, I. Chernyakhovskiy, K. Xu, S. Gadzanku and K. Coney, USAID GRID-SCALE ENERGY STORAGE TECHNOLOGIES PRIMER. [Online]. Available: <https://www.nrel.gov/publications>.
- 10 J. Noack, N. Roznyatovskaya, T. Herr and P. Fischer, The Chemistry of Redox-Flow Batteries, *Angew. Chem., Int. Ed.*, 2015, **54**, 9776–9809, DOI: [10.1002/anie.201410823](https://doi.org/10.1002/anie.201410823).
- 11 M. L. Perry and A. Z. Weber, Advanced Redox-Flow Batteries: A Perspective, *J. Electrochem. Soc.*, 2016, **163**(1), A5064–A5067, DOI: [10.1149/2.0101601jes](https://doi.org/10.1149/2.0101601jes).
- 12 Rongke Power (RKP), Rongke Power Completes 100 MW/400 MWh Vanadium Flow Battery Project in Cold-Climate Region, <https://rpkstorage.com/2024/12/25/rongke-power-completes-100mw-400mwh-vanadium-flow-battery-project-in-cold-climate-region/>.
- 13 D. G. Ivey, Bifunctional electrocatalysts for Zn–air batteries, *Sustainable Energy Fuels*, 2017, **2**, 39–67, DOI: [10.1039/C7SE00413C](https://doi.org/10.1039/C7SE00413C).
- 14 J. N. Liu, C. X. Zhao, J. Wang, D. Ren, B. Q. Li and Q. Zhang, A brief history of zinc–air batteries: 140 years of epic adventures, *Energy and Environ. Sci.*, 2022, **15**, 4542–4553, DOI: [10.1039/d2ee02440c](https://doi.org/10.1039/d2ee02440c).
- 15 N. E. Idoine, *et al.*, *British Geological Survey World Mineral Production*, 2023.
- 16 A. Eftekhari, On the Theoretical Capacity/Energy of Lithium Batteries and Their Counterparts, *ACS Sustainable Chem. Eng.*, 2018, **7**, 3684–3687, DOI: [10.1021/acsschemeng.7b04330](https://doi.org/10.1021/acsschemeng.7b04330).
- 17 N. E. I. L. E. Hetherington, T. J. Brown, A. J. Benham, P. A. J. Lusty, V. L. Hards and S. D. Hannis, *World Mineral Production*, British Geological Survey 2008, 2006.
- 18 G. J. May, A. Davidson and B. Monahov, Lead batteries for utility energy storage: a review, *J. Energy Storage*, 2018, **15**, 145–157, DOI: [10.1016/j.est.2017.11.008](https://doi.org/10.1016/j.est.2017.11.008).
- 19 B. Amunátegui, A. Ibáñez, M. Sierra and M. Pérez, Electrochemical energy storage for renewable energy integration: zinc–air flow batteries, *J. Appl. Electrochem.*, 2018, **48**(6), 627–637, DOI: [10.1007/s10800-017-1133-7](https://doi.org/10.1007/s10800-017-1133-7).
- 20 Duracell, Duracell: Technical/OEM, 2004.
- 21 Energizer Battery Manufacturing, Energizer Zinc Air Prismatic Handbook Including performance and design data for the PP355.
- 22 J. Pan, *et al.*, Preliminary study of alkaline single flowing Zn–O<sub>2</sub> battery, *Electrochem. Commun.*, 2009, **11**, 2191–2194, DOI: [10.1016/j.elecom.2009.09.028](https://doi.org/10.1016/j.elecom.2009.09.028).
- 23 S. Hosseini, W. Lao-atiman, S. J. Han, A. Arpornwichanop, T. Yonezawa and S. Kheawhom, Discharge Performance of Zinc–Air Flow Batteries Under the Effects of Sodium Dodecyl Sulfate and Pluronic F-127, *Sci. Rep.*, 2018, **8**(1), 14909, DOI: [10.1038/s41598-018-32806-3](https://doi.org/10.1038/s41598-018-32806-3).
- 24 W. Lao-atiman, K. Bumroongsil and A. Arpornwichanop, Model-Based Analysis of an Integrated Zinc–Air Flow Battery/Zinc Electrolyzer System, *Front. Energy Res.*, 2019, **7**, 1–15, DOI: [10.3389/fenrg.2019.00015](https://doi.org/10.3389/fenrg.2019.00015).
- 25 N. H. Choi, D. Del Olmo, P. Fischer, K. Pinkwart and J. Tübke, Development of flow fields for zinc slurry air flow batteries, *Batteries*, 2020, **6**(1), 1–10, DOI: [10.3390/batteries6010015](https://doi.org/10.3390/batteries6010015).
- 26 N. H. Choi, D. del Olmo, D. Milian, N. El Kissi, P. Fischer, K. Pinkwart and J. Tubke, Use of carbon additives towards rechargeable zinc slurry air flow batteries, *Energies*, 2020, **13**(17), 4482, DOI: [10.3390/en13174482](https://doi.org/10.3390/en13174482).
- 27 D. Pletcher, X. Li, S. W. T. Price, A. E. Russell, T. Sönmez and S. J. Thompson, Comparison of the Spinel Co<sub>3</sub>O<sub>4</sub> and NiCo<sub>2</sub>O<sub>4</sub> as Bifunctional Oxygen Catalysts in Alkaline Media, *Electrochim. Acta*, 2016, **188**, 286–293, DOI: [10.1016/j.electacta.2015.10.020](https://doi.org/10.1016/j.electacta.2015.10.020).
- 28 J. W. F. To, *et al.*, High-performance oxygen reduction and evolution carbon catalysis: from mechanistic studies to device integration, *Nano Res.*, 2017, **10**(4), 1163–1177, DOI: [10.1007/s12274-016-1347-8](https://doi.org/10.1007/s12274-016-1347-8).
- 29 X.-Z. Yuan, W. Qu, X. Zhang, P. Yao and J. Fahlman, Spinel Ni<sub>x</sub>Co<sub>2-x</sub>O<sub>4</sub> as a bifunctional air electrode for zinc–air batteries, *ECS Trans.*, 2013, **45**(29), 105–112.
- 30 S. Dresp, F. Luo, R. Schmack, S. Ku, M. Gliech and P. Strasser, An efficient bifunctional two-component catalyst for oxygen reduction and oxygen evolution in reversible fuel cells, electrolyzers and rechargeable air electrodes, *Energy Environ. Sci.*, 2016, **9**, 2020–2024, DOI: [10.1039/c6ee01046f](https://doi.org/10.1039/c6ee01046f).
- 31 N. Bogolowski, O. Ngaleu, M. Sakthivel and J. Drillet, Long-life bifunctional BaSrCoFeO<sub>3</sub>/C gas diffusion electrode, *Carbon*, 2017, **119**, 511–518, DOI: [10.1016/j.carbon.2017.04.051](https://doi.org/10.1016/j.carbon.2017.04.051).
- 32 M. Bockelmann, U. Kunz and T. Turek, Electrically rechargeable zinc-oxygen flow battery with high power density, *Electrochem. Commun.*, 2016, **69**, 24–27, DOI: [10.1016/j.elecom.2016.05.013](https://doi.org/10.1016/j.elecom.2016.05.013).
- 33 L. Li, C. Liu, G. He, D. Fan and A. Manthiram, Hierarchical pore-in-pore and wire-in-wire catalysts for rechargeable



- Zn- and Li-air batteries with ultra-long cycle life and high cell efficiency, *Energy Environ. Sci.*, 2015, **8**(11), 3274–3282, DOI: [10.1039/c5ee02616d](https://doi.org/10.1039/c5ee02616d).
- 34 Zinc8 Energy solutions, Zinc8 energy storage system: How it works.
- 35 J. Yi, P. Liang, X. Liu, K. Wu, Y. Liu, Y. Wang, Y. Xia and J. Zhang, Challenges, mitigation strategies and perspectives in development of zinc-electrode materials and fabrication for rechargeable zinc-air batteries, *Energy Environ. Sci.*, 2018, **11**, 3075–3095, DOI: [10.1039/c8ee01991f](https://doi.org/10.1039/c8ee01991f).
- 36 K. Roy, A. Rana, J. N. Heil, B. M. Tackett and J. E. Dick, For Zinc Metal Batteries, How Many Electrons go to Hydrogen Evolution? An Electrochemical Mass Spectrometry Study, *Angew. Chem., Int. Ed.*, 2024, **63**(11), e202319010, DOI: [10.1002/anie.202319010](https://doi.org/10.1002/anie.202319010).
- 37 M. Pourbaix, *Atlas of electrochemical equilibria in aqueous solutions*, Pergamon Press Ltd, 1966.
- 38 C. J. Lan, T. S. Chin, P. H. Lin and T. P. Perng, Zn–Al alloy as a new anode-metal of a zinc–air battery Zn–Al alloy as a new anode-metal of a zinc–air battery, *J. New Mater. Electrochem. Syst.*, 2006, **9**, 27–32.
- 39 A.-R. El-Sayed, H. S. Mohran and H. M. Abd El-Lateef, Corrosion Study of Zinc, Nickel, and Zinc–Nickel Alloys in Alkaline Solutions by Tafel Plot and Impedance Techniques, *Metall Mater. Trans. A*, 2012, **43**(2), 619, DOI: [10.1016/S1003-6326\(15\)63906-1](https://doi.org/10.1016/S1003-6326(15)63906-1).
- 40 C. Woo, K. Sathiyarayanan, S. Wook and M. Soo, Novel alloys to improve the electrochemical behavior of zinc anodes for zinc/air battery, *J. Power Sources*, 2006, **160**, 1436–1441, DOI: [10.1016/j.jpowsour.2006.02.019](https://doi.org/10.1016/j.jpowsour.2006.02.019).
- 41 K. Kim, Y. Cho, S. Wook, H. Kim and J. Hyun, Anions of organic acids as gas suppressants in zinc–air batteries, *Mater. Res. Bull.*, 2010, **45**(3), 262–264, DOI: [10.1016/j.materresbull.2009.06.020](https://doi.org/10.1016/j.materresbull.2009.06.020).
- 42 S. Lee, Y. Kim, S. Eom, N. Choi, K. Kim and S. Cho, Improvement in self-discharge of Zn anode by applying surface modification for Zn–air batteries with high energy density, *J. Power Sources*, 2013, **227**, 177–184, DOI: [10.1016/j.jpowsour.2012.11.046](https://doi.org/10.1016/j.jpowsour.2012.11.046).
- 43 Y. Cho and G. T. Fey, Surface treatment of zinc anodes to improve discharge capacity and suppress hydrogen gas evolution, *J. Power Sources*, 2008, **184**, 610–616, DOI: [10.1016/j.jpowsour.2008.04.081](https://doi.org/10.1016/j.jpowsour.2008.04.081).
- 44 F. W. Thomas Goh, *et al.*, A Near-Neutral Chloride Electrolyte for Electrically Rechargeable Zinc–Air Batteries, *J. Electrochem. Soc.*, 2014, **161**(14), A2080–A2086, DOI: [10.1149/2.0311414jes](https://doi.org/10.1149/2.0311414jes).
- 45 S. Lysgaard, M. K. Christensen, H. A. Hansen, J. Maria, P. Norby and T. Vegge, Combined DFT and Differential Electrochemical Mass Spectrometry Investigation of the Effect of Dopants in Secondary Zinc–Air Batteries, *ChemSusChem*, 2018, **1**, 1933–1941, DOI: [10.1002/cssc.201800225](https://doi.org/10.1002/cssc.201800225).
- 46 M. Auinat and D. Starosvetsky, Electrochemical and surface studies of zinc in alkaline solutions containing organic corrosion inhibitors, *J. Power Sources*, 2003, **114**, 330–337.
- 47 N. A. Hampson and M. J. Tarbox, The Anodic Behavior of Zinc in Potassium Hydroxide Solution: I. Horizontal Anodes, *J. Electrochem. Soc.*, 1963, **110**, 95.
- 48 G. Davies, A. G. Hsieh, M. Hultmark, M. E. Mueller and D. A. Steingart, Utilization of Hyper-Dendritic Zinc during High Rate Discharge in Alkaline Electrolytes, *J. Electrochem. Soc.*, 2016, **163**(7), A1340–A1347, DOI: [10.1149/2.0891607jes](https://doi.org/10.1149/2.0891607jes).
- 49 A. R. Mainar, *et al.*, An overview of progress in electrolytes for secondary zinc–air batteries and other storage systems based on zinc, *J. Energy Storage*, 2018, **15**, 304–328, DOI: [10.1016/j.est.2017.12.004](https://doi.org/10.1016/j.est.2017.12.004).
- 50 R. D. Naybur, The effect of electrolyte flow on the morphology of zinc electrodeposited from aqueous alkaline solution containing zincate ions, *J. Electrochem. Soc.*, 1969, **116**(4), 520–524, DOI: [10.1016/j.apenergy.2014.04.095](https://doi.org/10.1016/j.apenergy.2014.04.095).
- 51 S. Amendola, US 2012/0021303 A1, 2012.
- 52 S. J. Banik and R. Akolkar, Suppressing Dendritic Growth during Alkaline Zinc Electrodeposition using Polyethylenimine Additive, *Electrochim. Acta*, 2015, **179**, 475–481, DOI: [10.1016/j.electacta.2014.12.100](https://doi.org/10.1016/j.electacta.2014.12.100).
- 53 M. Cifraín and K. V. Kordesch, Advances, aging mechanism and lifetime in AFCs with circulating electrolytes, *J. Power Sources*, 2004, 234–242, DOI: [10.1016/j.jpowsour.2003.09.019](https://doi.org/10.1016/j.jpowsour.2003.09.019).
- 54 N. Fujiwara, M. Yao, Z. Siroma, H. Senoh, T. Ioroi and K. Yasuda, Reversible air electrodes integrated with an anion-exchange membrane for secondary air batteries, *J. Power Sources*, 2011, **196**, 808–813, DOI: [10.1016/j.jpowsour.2010.07.074](https://doi.org/10.1016/j.jpowsour.2010.07.074).
- 55 A. Sumboja, *et al.*, Durable rechargeable zinc–air batteries with neutral electrolyte and manganese oxide catalyst, *J. Power Sources*, 2016, **332**, 330–336, DOI: [10.1016/j.jpowsour.2016.09.142](https://doi.org/10.1016/j.jpowsour.2016.09.142).
- 56 S. Garg, *et al.*, How alkali cations affect salt precipitation and CO<sub>2</sub> electrolysis performance in membrane electrode assembly electrolyzers, *Energy Environ. Sci.*, 2023, **16**(4), 1631–1643, DOI: [10.1039/d2ee03725d](https://doi.org/10.1039/d2ee03725d).
- 57 M. T. Tsehaye, *et al.*, Anion Exchange Membranes Incorporating Multi N-Spirocyclic Quaternary Ammonium Cations via Ultraviolet-Initiated Polymerization for Zinc Slurry-Air Flow Batteries, *ACS Appl. Energy Mater.*, 2022, **5**(6), 7069–7080, DOI: [10.1021/acsaem.2c00697](https://doi.org/10.1021/acsaem.2c00697).
- 58 M. T. Tsehaye, F. Alloin and C. Iojoiu, Prospects for anion-exchange membranes in alkali metal–air batteries, *Energies*, 2019, **15**, 4702, DOI: [10.3390/en12244702](https://doi.org/10.3390/en12244702).
- 59 B. H. Lim, *et al.*, Comparison of catalyst-coated membranes and catalyst-coated substrate for PEMFC membrane electrode assembly: a review, *Chin. J. Chem. Eng.*, 2021, **33**, 1–16, DOI: [10.1016/j.cjche.2020.07.044](https://doi.org/10.1016/j.cjche.2020.07.044).
- 60 K. Xu, A. Loh, B. Wang and X. Li, Enhancement of Oxygen Transfer by Design Nickel Foam Electrode for Zinc–Air Battery, *J. Electrochem. Soc.*, 2018, **165**(5), A809–A818, DOI: [10.1149/2.0361805jes](https://doi.org/10.1149/2.0361805jes).
- 61 S. W. T. Price, *et al.*, The fabrication of a bifunctional oxygen electrode without carbon components for alkaline



- secondary batteries, *J. Power Sources*, 2014, **259**, 43–49, DOI: [10.1016/j.jpowsour.2014.02.058](https://doi.org/10.1016/j.jpowsour.2014.02.058).
- 62 A. R. Mainar, *et al.*, High performance carbon free bifunctional air electrode for advanced zinc–air batteries, *Electrochim. Acta*, 2023, **446**, 142075, DOI: [10.1016/j.electacta.2023.142075](https://doi.org/10.1016/j.electacta.2023.142075).
- 63 Y. Yi, *et al.*, Electrochemical corrosion of a glassy carbon electrode, *Catal. Today*, 2017, **295**, 32–40, DOI: [10.1016/j.cattod.2017.07.013](https://doi.org/10.1016/j.cattod.2017.07.013).
- 64 N. Bogolowski, O. Ngaleu, M. Sakthivel and J. Drillet, Long-life bifunctional BaSrCoFeO<sub>3</sub>/C gas diffusion electrode, *Carbon*, 2017, **119**, 511–518, DOI: [10.1016/j.carbon.2017.04.051](https://doi.org/10.1016/j.carbon.2017.04.051).
- 65 K. Wang, P. Pei, Z. Ma, H. Xu, P. Li and X. Wang, Morphology control of zinc regeneration for zinc–air fuel cell and battery, *J. Power Sources*, 2014, **271**, 65–75, DOI: [10.1016/j.jpowsour.2014.07.182](https://doi.org/10.1016/j.jpowsour.2014.07.182).
- 66 K. N. Grew, X. Ren and D. Chu, Effects of temperature and carbon dioxide on anion exchange membrane conductivity, *Electrochem. Solid-State Lett.*, 2011, **14**, 12, DOI: [10.1149/2.011112esl](https://doi.org/10.1149/2.011112esl).
- 67 D. Schröder, N. N. Sinai Borker, M. König and U. Krewer, Performance of zinc air batteries with added K<sub>2</sub>CO<sub>3</sub> in the alkaline electrolyte, *J. Appl. Electrochem.*, 2015, **45**, 427–437, DOI: [10.1007/s10800-015-0817-0](https://doi.org/10.1007/s10800-015-0817-0).
- 68 J. F. Drillet, F. Holzer, T. Kallis, S. Müller and V. M. Schmidt, Influence of CO<sub>2</sub> on the stability of bifunctional oxygen electrodes for rechargeable zinc/air batteries and study of different CO<sub>2</sub> filter materials, *Phys. Chem. Chem. Phys.*, 2001, 368–371, DOI: [10.1039/b005523i](https://doi.org/10.1039/b005523i).
- 69 T. Burchardt and M. Lanfrancioni, *Ionic liquid reduced carbonation*, WO2011013004A1, 2011.
- 70 M. Suermann, T. J. Schmidt and F. N. Büchi, Investigation of Mass Transport Losses in Polymer Electrolyte Electrolysis Cells, *ECS Trans.*, 2015, **69**(17), 1141–1148, DOI: [10.1149/06917.1141ecst](https://doi.org/10.1149/06917.1141ecst).
- 71 K. E. Ayers, *et al.*, Research Advances towards Low Cost, High Efficiency PEM Electrolysis, *ECS Trans.*, 2010, **33**(1), 3–15, DOI: [10.1149/1.3484496](https://doi.org/10.1149/1.3484496).
- 72 M. Bernt, H. A. Gasteiger and J. E. Soc, Influence of Ionomer Content in IrO<sub>2</sub>/TiO<sub>2</sub> Electrodes on PEM Water Electrolyzer Performance, *J. Electrochem. Soc.*, 2016, **136**(11), F3179–F3189, DOI: [10.1149/2.023161jes](https://doi.org/10.1149/2.023161jes).
- 73 A. Badgett, M. Ruth and B. Pivovar, Economic considerations for hydrogen production with a focus on polymer electrolyte membrane electrolysis, *Electrochemical Power Sources: Fundamentals, Systems, and Applications Hydrogen Production by Water Electrolysis*, Elsevier, 2021, pp. 327–364, DOI: [10.1016/B978-0-12-819424-9.00005-7](https://doi.org/10.1016/B978-0-12-819424-9.00005-7).
- 74 F. Du, *et al.*, Effects of PEMFC Operational History under Dry/Wet Conditions on Additional Voltage Losses due to Ionomer Migration, *J. Electrochem. Soc.*, 2020, **167**(14), 144513, DOI: [10.1149/1945-7111/abc83f](https://doi.org/10.1149/1945-7111/abc83f).
- 75 Hydrogen Storage Technologies Roadmap Fuel Cell Technical Team Roadmap, 2017, [Online]. Available: <https://www.uscar.org>.
- 76 M. Schalenbach, M. Carmo, D. L. Fritz, J. Mergel and D. Stolten, Pressurized PEM water electrolysis: efficiency and gas crossover, *Int. J. Hydrogen Energy*, 2013, **38**(35), 14921–14933, DOI: [10.1016/j.ijhydene.2013.09.013](https://doi.org/10.1016/j.ijhydene.2013.09.013).
- 77 R. Hancke, T. Holm and Ø. Ulleberg, The case for high-pressure PEM water electrolysis, *Energy Convers. Manage.*, 2022, **261**, 115642, DOI: [10.1016/j.enconman.2022.115642](https://doi.org/10.1016/j.enconman.2022.115642).
- 78 C. Wei, *et al.*, Recommended Practices and Benchmark Activity for Hydrogen and Oxygen Electrocatalysis in Water Splitting and Fuel Cells, *Adv. Mater.*, 2019, **1806296**, 1–24, DOI: [10.1002/adma.201806296](https://doi.org/10.1002/adma.201806296).
- 79 M. Busch, N. B. Halck, U. I. Kramm, S. Siahrostami, P. Krtil and J. Rossmeisl, Beyond the top of the volcano? – A unified approach to electrocatalytic oxygen reduction and oxygen evolution, *Nano Energy*, 2016, **29**, 126–135, DOI: [10.1016/j.nanoen.2016.04.011](https://doi.org/10.1016/j.nanoen.2016.04.011).
- 80 T. Schuler, J. Ciccone, B. Krentscher, F. Marone, C. Peter, T. Schmidt and F. Büchi, Hierarchically Structured Porous Transport Layers for Polymer Electrolyte Water Electrolysis, *Adv. Energy Mater.*, 2020, **10**(2), 1903216, DOI: [10.1002/aenm.201903216](https://doi.org/10.1002/aenm.201903216).
- 81 X. Z. Yuan, N. Shaigan, C. Song, M. Aujla, V. Naburchilov, J. Kwan, D. Wilkinson, A. Bazylak and K. Fatih, The porous transport layer in proton exchange membrane water electrolysis: perspectives on a complex component, *Sustainable Energy Fuels*, 2022, **6**, 1824–1853, DOI: [10.1039/d2se00260d](https://doi.org/10.1039/d2se00260d).
- 82 J. E. Park, H. Choi, S. Kang, G. Jang, O. Kim, M. Karuppannan, Y. Sung, O. Kwon and Y. Cho, Effect of pore structures in nickel-based porous transport layers for high-performance and durable anion-exchange membrane water electrolysis, *Int. J. Energy Res.*, 2022, **46**, 16670–16678, DOI: [10.1002/er.8331](https://doi.org/10.1002/er.8331).
- 83 N. U. Hassan, E. Motyka, J. Kweder, P. Ganesan, B. Brechin, B. Zulevi, H. Colon-Mercado, P. Kohl and W. Mustain, Effect of porous transport layer properties on the anode electrode in anion exchange membrane electrolyzers, *J. Power Sources*, 2023, **555**, 232371, DOI: [10.1016/j.jpowsour.2022.232371](https://doi.org/10.1016/j.jpowsour.2022.232371).
- 84 S. W. T. Price, S. J. Thompson, X. Li and S. F. Gorman, The Fabrication of a Bifunctional Oxygen GDE without Carbon Components for Alkaline Secondary Batteries, *J. Power Sources*, 2014, **259**, 43–49, DOI: [10.1016/j.jpowsour.2014.02.058](https://doi.org/10.1016/j.jpowsour.2014.02.058).
- 85 Y. Zhou, *et al.*, Significance of Engineering the Octahedral Units to Promote the Oxygen Evolution Reaction of Spinel Oxides, *Adv. Mater.*, 2019, **31**(41), 1–11, DOI: [10.1002/adma.201902509](https://doi.org/10.1002/adma.201902509).
- 86 C. Wei, Z. Feng, G. G. Scherer, J. Barber, Y. Shao-horn and Z. J. Xu, Cations in Octahedral Sites: A Descriptor for Oxygen Electrocatalysis on Transition-Metal Spinel, *Adv. Mater.*, 2017, **29**, 1606800, DOI: [10.1002/adma.201606800](https://doi.org/10.1002/adma.201606800).
- 87 Z. Chen, A. Yu, D. Higgins, H. Li, H. Wang and Z. Chen, Highly Active and Durable Core–Corona Structured Bifunctional Catalyst for Rechargeable Metal–Air Battery Application, *Nano Lett.*, 2012, **12**, 1946–1952, DOI: [10.1021/nl2044327](https://doi.org/10.1021/nl2044327).
- 88 I. S. Filimonenkov, C. Bouillet, G. Kéranguéven, P. A. Simonov, G. A. Tsirlina and E. R. Savinova, Carbon



- materials as additives to the OER catalysts: RRDE study of carbon corrosion at high anodic potentials, *Electrochim. Acta*, 2019, **321**, 134657, DOI: [10.1016/j.electacta.2019.134657](https://doi.org/10.1016/j.electacta.2019.134657).
- 89 T. Wang, Z. Shi, F. Wang, J. He, Y. Zhong, Y. Ma, Z. Zhu, X. Cheng, K. Ozoemena and Y. Wu, Advanced bifunctional catalyst design for rechargeable zinc–air batteries, *EES Catal.*, 2024, **3**, 696–726, DOI: [10.1039/d4ey00014e](https://doi.org/10.1039/d4ey00014e).
- 90 X. Zhu, C. Hu, R. Amal, L. Dai and X. Lu, Heteroatom-doped carbon catalysts for zinc–air batteries: progress, mechanism, and opportunities, *Energy Environ. Sci.*, 2020, **13**, 4536, DOI: [10.1039/d0ee02800b](https://doi.org/10.1039/d0ee02800b).
- 91 V. Neburchilov, H. Wang, J. J. Martin and W. Qu, A review on air cathodes for zinc–air fuel cells, *J. Power Sources*, 2010, **195**, 1271–1291, DOI: [10.1016/j.jpowsour.2009.08.100](https://doi.org/10.1016/j.jpowsour.2009.08.100).
- 92 Y. Pei, D. P. Wilkinson and E. Gyenge, Insights into the Electrochemical Behavior of Manganese Oxides as Catalysts for the Oxygen Reduction and Evolution Reactions: Monometallic Core–Shell Mn/Mn<sub>3</sub>O<sub>4</sub>, *Small*, 2023, **19**(19), 2204585, DOI: [10.1002/sml.202204585](https://doi.org/10.1002/sml.202204585).
- 93 C. Zhou, *et al.*, Superdurable Bifunctional Oxygen Electrocatalyst for High-Performance zinc–air Batteries, *J. Am. Chem. Soc.*, 2022, **144**(6), 2694–2704, DOI: [10.1021/jacs.1c11675](https://doi.org/10.1021/jacs.1c11675).
- 94 G. C. Silva, S. Cherevko, K. J. J. Mayrhofer and E. A. Ticianelli, Dissolution Stability: The Major Challenge in the Regenerative Fuel Cells Bifunctional Catalysis, *J. Electrochem. Soc.*, 2018, **165**(16), F1376–F1384, DOI: [10.1149/2.1201816jes](https://doi.org/10.1149/2.1201816jes).
- 95 H. Li, *et al.*, Active Phase on SrCo<sub>1-x</sub>Fe<sub>x</sub>O<sub>3-δ</sub> (0 ≤ x ≤ 0.5) Perovskite for Water Oxidation: Reconstructed Surface versus Remaining Bulk, *JACS Au*, 2021, **1**(1), 108–115, DOI: [10.1021/jacsau.0c00022](https://doi.org/10.1021/jacsau.0c00022).
- 96 F. D. Speck, P. G. Santori, F. Jaouen and S. Cherevko, Mechanisms of Manganese Oxide Electrocatalysts Degradation during Oxygen Reduction and Oxygen Evolution Reactions, *J. Phys. Chem. C*, 2019, **123**(41), 25267–25277, DOI: [10.1021/acs.jpcc.9b07751](https://doi.org/10.1021/acs.jpcc.9b07751).
- 97 J. Huang, S. B. Scott, I. Chorkendorff and Z. Wen, Online Electrochemistry-Mass Spectrometry Evaluation of the Acidic Oxygen Evolution Reaction at Supported Catalysts, *ACS Catal.*, 2021, **11**(20), 12745–12753, DOI: [10.1021/acscatal.1c03430](https://doi.org/10.1021/acscatal.1c03430).
- 98 E. Bertheussen, Y. Abghoui, Z. P. Jovanov and A. Varela, Quantification of liquid products from the electroreduction of CO<sub>2</sub> and CO using static headspace-gas chromatography and nuclear magnetic resonance spectroscopy, *Catal. Today*, 2017, **288**, 54–62, DOI: [10.1016/j.cattod.2017.02.029](https://doi.org/10.1016/j.cattod.2017.02.029).
- 99 S. Cherevko, Stability and dissolution of electrocatalysts: building the bridge between model and ‘real world’ systems, *Curr. Opin. Electrochem.*, 2018, **8**, 118–125, DOI: [10.1016/j.coelec.2018.03.034](https://doi.org/10.1016/j.coelec.2018.03.034).
- 100 E. Fabbri, *et al.*, Dynamic surface self-reconstruction is the key of highly active perovskite nano-electrocatalysts for water splitting, *Nat. Mater.*, 2017, **16**(9), 925–931, DOI: [10.1038/nmat4938](https://doi.org/10.1038/nmat4938).
- 101 T. Wu, *et al.*, Iron-facilitated dynamic active-site generation on spinel CoAl<sub>2</sub>O<sub>4</sub> with self-termination of surface reconstruction for water oxidation, *Nat. Catal.*, 2019, **2**(9), 763–772, DOI: [10.1038/s41929-019-0325-4](https://doi.org/10.1038/s41929-019-0325-4).
- 102 International Renewable Energy Agency, *Electricity storage and renewables: costs and markets to 2030*, 2017th edn.
- 103 H. A. Gasteiger, S. S. Kocha, B. Sompalli and F. T. Wagner, Activity benchmarks and requirements for Pt, Pt-alloy, and non-Pt oxygen reduction catalysts for PEMFCs, *Appl. Catal., B*, 2005, **56**(1–2), 9–35, DOI: [10.1016/j.apcatb.2004.06.021](https://doi.org/10.1016/j.apcatb.2004.06.021).
- 104 P. C. K. Vesborg and T. F. Jaramillo, Addressing the terawatt challenge: scalability in the supply of chemical elements for renewable energy, *RSC Adv.*, 2012, **2**(21), 7933–7947, DOI: [10.1039/c2ra20839c](https://doi.org/10.1039/c2ra20839c).
- 105 J. Suntivich, H. A. Gasteiger and N. Yabuuchi, Electrocatalytic Measurement Methodology of Oxide Catalysts Using a Thin-Film Rotating Disk Electrode, *J. Electrochem. Soc.*, 2010, **157**(8), 1263–1268, DOI: [10.1149/1.3456630](https://doi.org/10.1149/1.3456630).
- 106 H. A. Gasteiger, S. S. Kocha, B. Sompalli and F. T. Wagner, Activity benchmarks and requirements for Pt, Pt-alloy, and non-Pt oxygen reduction catalysts for PEMFCs, *Appl. Catal., B*, 2005, **56**, 9–35, DOI: [10.1016/j.apcatb.2004.06.021](https://doi.org/10.1016/j.apcatb.2004.06.021).
- 107 S. Dressp and P. Strasser, Non-Noble Metal Oxides and their Application as Bifunctional Catalyst in Reversible Fuel Cells and Rechargeable Air Batteries, *ChemCatChem*, 2018, **10**(18), 4162–4171, DOI: [10.1002/cctc.201800660](https://doi.org/10.1002/cctc.201800660).
- 108 C. Roy, *et al.*, Impact of nanoparticle size and lattice oxygen on water oxidation on NiFeO, *Nat. Catal.*, 2018, **1**, 820–829, DOI: [10.1038/s41929-018-0162-x](https://doi.org/10.1038/s41929-018-0162-x).
- 109 F. Dionigi, *et al.*, In-situ structure and catalytic mechanism of NiFe and CoFe layered double hydroxides during oxygen evolution, *Nat. Commun.*, 2020, **11**(1), 1–10, DOI: [10.1038/s41467-020-16237-1](https://doi.org/10.1038/s41467-020-16237-1).
- 110 D. Xu, *et al.*, Earth-Abundant Oxygen Electrocatalysts for Alkaline Anion-Exchange-Membrane Water Electrolysis: Effects of Catalyst Conductivity and Comparison with Performance in Three-Electrode Cells, *ACS Catal.*, 2019, **9**(1), 7–15, DOI: [10.1021/acscatal.8b04001](https://doi.org/10.1021/acscatal.8b04001).
- 111 K. A. Stoerzinger, M. Risch, B. Han and Y. Shao-horn, Recent Insights into Manganese Oxides in Catalyzing Oxygen Reduction Kinetics, *ACS Catal.*, 2015, **5**, 6021–6031, DOI: [10.1021/acscatal.5b01444](https://doi.org/10.1021/acscatal.5b01444).
- 112 A. R. Mainar, *et al.*, Manganese oxide catalysts for secondary zinc air batteries: from electrocatalytic activity to bifunctional air electrode performance, *Electrochim. Acta*, 2016, **217**, 80–91, DOI: [10.1016/j.electacta.2016.09.052](https://doi.org/10.1016/j.electacta.2016.09.052).
- 113 M. Risch, K. A. Stoerzinger, S. Maruyama, W. T. Hong, I. Takeuchi and Y. Shao-horn, La<sub>0.8</sub>Sr<sub>0.2</sub>MnO<sub>3</sub> decorated with Ba<sub>0.5</sub>Sr<sub>0.5</sub>Co<sub>0.8</sub>Fe<sub>0.2</sub>O<sub>3</sub>: a Bi-functional Surface for Oxygen Electrocatalysis with Enhanced Stability and Activity, *J. Am. Chem. Soc.*, 2014, **136**(14), 5229–5232, DOI: [10.1021/ja5009954](https://doi.org/10.1021/ja5009954).
- 114 W. T. Hong, M. Risch, K. A. Stoerzinger, A. Grimaud, J. Suntivich and Y. Shao-Horn, Toward the rational design of non-precious transition metal oxides for oxygen



- electrocatalysis, *Energy Environ. Sci.*, 2015, **8**(5), 1404–1427, DOI: [10.1039/c4ee03869j](https://doi.org/10.1039/c4ee03869j).
- 115 S. J. Thompson, S. W. T. Price, D. Pletcher and A. E. Russell, Voltammetric Studies of the Mechanism of the Oxygen Reduction in Alkaline Media at the Spinels  $\text{Co}_3\text{O}_4$  and  $\text{NiCo}_2\text{O}_4$ , *J. Electrochem. Soc.*, 2016, **163**(10), H884–H890, DOI: [10.1149/2.0111610jes](https://doi.org/10.1149/2.0111610jes).
- 116 W. Sheng, H. A. Gasteiger and Y. Shao-horn, Hydrogen Oxidation and Evolution Reaction Kinetics on Platinum: Acid vs. Alkaline Electrolytes, *J. Electrochem. Soc.*, 2010, **157**(11), B1529–B1536, DOI: [10.1149/1.3483106](https://doi.org/10.1149/1.3483106).
- 117 Y. Lee, J. Suntivich, K. J. May, E. E. Perry and Y. Shao-horn, Synthesis and Activities of Rutile  $\text{IrO}_2$  and  $\text{RuO}_2$  Nanoparticles for Oxygen Evolution in Acid and Alkaline Solutions, *J. Phys. Chem. Lett.*, 2012, **3**, 399–404.
- 118 W. Sheng, H. A. Gasteiger and Y. Shao-horn, Hydrogen Oxidation and Evolution Reaction Kinetics on Platinum: Acid vs. Alkaline Electrolytes, *J. Electrochem. Soc.*, 2010, **157**(11), B1529–B1536, DOI: [10.1149/1.3483106](https://doi.org/10.1149/1.3483106).
- 119 A. Indra, *et al.*, Unification of Catalytic Water Oxidation and Oxygen Reduction Reactions: Amorphous Beat Crystalline Cobalt Iron Oxides, *J. Am. Chem. Soc.*, 2014, **136**, 17530–17536, DOI: [10.1021/ja509348t](https://doi.org/10.1021/ja509348t).
- 120 P. W. Menezes, A. Indra, R. Sahraie and A. Bergmann, Cobalt – Manganese-Based Spinels as Multifunctional Materials that Unify Catalytic Water Oxidation and Oxygen Reduction Reactions, *ChemSusChem*, 2015, 164–171, DOI: [10.1002/cssc.201402699](https://doi.org/10.1002/cssc.201402699).
- 121 J. K. Nørskov, *et al.*, Origin of the Overpotential for Oxygen Reduction at a Fuel-Cell Cathode, *J. Phys. Chem.*, 2004, **108**, 17886–17892, DOI: [10.1021/jp047349j](https://doi.org/10.1021/jp047349j).
- 122 I. C. Man, *et al.*, Universality in Oxygen Evolution Electrocatalysis on Oxide Surfaces, *ChemCatChem*, 2011, **3**, 1159–1165, DOI: [10.1002/cctc.201000397](https://doi.org/10.1002/cctc.201000397).
- 123 M. T. M. Koper, Thermodynamic theory of multi-electron transfer reactions: implications for electrocatalysis, *J. Electroanal. Chem.*, 2011, **660**(2), 254–260.
- 124 J. Suntivich, K. J. May, H. A. Gasteiger, J. B. Goodenough and Y. Shao-Horn, A Perovskite Oxide Optimized for Oxygen Evolution Catalysis from Molecular Orbital Principles, *Science*, 2011, **334**, 1383–1385.
- 125 J. Suntivich, H. A. Gasteiger, N. Yabuuchi, H. Nakanishi, J. B. Goodenough and Y. Shao-horn, Design principles for oxygen-reduction activity on perovskite oxide catalysts for fuel cells and metal – air batteries, *Nat. Chem.*, 2011, **3**(7), 546–550, DOI: [10.1038/nchem.1069](https://doi.org/10.1038/nchem.1069).
- 126 Y. Sun, *et al.*, Covalency competition dominates the water oxidation structure–activity relationship on spinel oxides, *Nat. Catal.*, 2020, **3**(7), 554–563, DOI: [10.1038/s41929-020-0465-6](https://doi.org/10.1038/s41929-020-0465-6).
- 127 A. Kulkarni, S. Siahrostami, A. Patel and J. K. Nørskov, Understanding Catalytic Activity Trends in the Oxygen Reduction Reaction, *Chem. Rev.*, 2018, **118**, 2302–2312, DOI: [10.1021/acs.chemrev.7b00488](https://doi.org/10.1021/acs.chemrev.7b00488).
- 128 Y. Peng, H. Hajiyani and R. Pentcheva, Influence of Fe and Ni doping on the oer performance at the  $\text{Co}_3\text{O}_4(001)$  surface: insights from DFT+*U* calculations, *ACS Catal.*, 2021, **11**(9), 5601–5613, DOI: [10.1021/acscatal.1c00214](https://doi.org/10.1021/acscatal.1c00214).
- 129 X. Sun, J. Sun, L. Guo, L. Hou and C. Yuan, Understanding the crystal structure-dependent electrochemical capacitance of spinel and rock-salt Ni–Co oxides: via density functional theory calculations, *RSC Adv.*, 2020, **10**(59), 35611–35618, DOI: [10.1039/d0ra05578f](https://doi.org/10.1039/d0ra05578f).
- 130 S. Yang, *et al.*, Toward the Decentralized Electrochemical Production of  $\text{H}_2\text{O}_2$ : A Focus on the Catalysis, *ACS Catal.*, 2018, **8**(5), 4064–4081, DOI: [10.1021/acscatal.8b00217](https://doi.org/10.1021/acscatal.8b00217).
- 131 Y. Duan, *et al.*, Mastering Surface Reconstruction of Metastable Spinel Oxides for Better Water Oxidation, *Adv. Mater.*, 2019, **31**(12), 2–9, DOI: [10.1002/adma.201807898](https://doi.org/10.1002/adma.201807898).
- 132 S. Divanis, T. Kutlusoy, I. M. Ingmer Boye, I. C. Man and J. Rossmeisl, Oxygen evolution reaction: a perspective on a decade of atomic scale simulations, *Chem. Sci.*, 2020, **11**(11), 2943–2950, DOI: [10.1039/c9sc05897d](https://doi.org/10.1039/c9sc05897d).
- 133 R. R. Rao, S. Corby, A. Bucci, M. Garcia-Tecedor, C. Mesa, J. Rossmeisl, S. Gimenez, J. Lloret-Fillol, I. Stephens and J. Durrant, Spectroelectrochemical Analysis of the Water Oxidation Mechanism on Doped Nickel Oxides, *J. Am. Chem. Soc.*, 2022, 7622–7633, DOI: [10.1021/jacs.1c08152](https://doi.org/10.1021/jacs.1c08152).
- 134 A. Bergmann, E. Martinez-Moreno, D. Teschner, P. Chernev, M. Gliech, J. De Araujo, T. Reier, H. Dau and P. Strasser, Reversible amorphization and the catalytically active state of crystalline  $\text{Co}_3\text{O}_4$  during oxygen evolution, *Nat. Commun.*, 2015, **6**, 8625, DOI: [10.1038/ncomms9625](https://doi.org/10.1038/ncomms9625).
- 135 Y. Gorlin, *et al.*, In Situ X-ray Absorption Spectroscopy Investigation of a Bifunctional Manganese Oxide Catalyst with High Activity for Electrochemical Water Oxidation and Oxygen Reduction, *J. Am. Chem. Soc.*, 2013, **135**, 8525–8534, DOI: [10.1021/ja310463z](https://doi.org/10.1021/ja310463z).
- 136 S. Corby, *et al.*, Separating bulk and surface processes in  $\text{NiO}_x$  electrocatalysts for water oxidation, *Sustainable Energy Fuels*, 2020, **4**(10), 5024–5030, DOI: [10.1039/d0se00977f](https://doi.org/10.1039/d0se00977f).
- 137 S. B. Scott, *et al.*, The low overpotential regime of acidic water oxidation part II: trends in metal and oxygen stability numbers, *Energy Environ. Sci.*, 2022, 1988–2001, DOI: [10.1039/d1ee03915f](https://doi.org/10.1039/d1ee03915f).
- 138 J. C. Meier, *et al.*, Design criteria for stable Pt/C fuel cell catalysts, *Beilstein J. Nanotechnol.*, 2014, **5**, 44–67, DOI: [10.3762/bjnano.5.5](https://doi.org/10.3762/bjnano.5.5).
- 139 J. M. Linge, V. Briega-Martos, A. Hutzler, B. Fritsch, H. Erikson, K. Tammeveski and S. Cherevko, Stability of Carbon Supported Silver Electrocatalysts for Alkaline Oxygen Reduction and Evolution Reactions, *ACS Appl. Energy Mater.*, 2023, **6**(22), 11497–11509, DOI: [10.1021/acsaem.3c01717](https://doi.org/10.1021/acsaem.3c01717).
- 140 C. Kuai, *et al.*, Phase segregation reversibility in mixed-metal hydroxide water oxidation catalysts, *Nat. Catal.*, 2020, **3**(9), 743–753, DOI: [10.1038/s41929-020-0496-z](https://doi.org/10.1038/s41929-020-0496-z).
- 141 M. L. Weber, *et al.*, Atomistic Insights into Activation and Degradation of  $\text{La}_{0.6}\text{Sr}_{0.4}\text{CoO}_{3-\delta}$  Electrocatalysts under Oxygen Evolution Conditions, *J. Am. Chem. Soc.*, 2022, **144**(39), 17966–17979, DOI: [10.1021/jacs.2c07226](https://doi.org/10.1021/jacs.2c07226).
- 142 L. Trotochaud, S. L. Young, J. K. Ranney and S. W. Boettcher, Nickel–Iron Oxyhydroxide Oxygen-Evolution



- Electrocatalysts: The Role of Intentional and Incidental Iron Incorporation, *J. Am. Chem. Soc.*, 2014, **136**, 6744–6753, DOI: [10.1021/ja502379c](https://doi.org/10.1021/ja502379c).
- 143 D. Y. Chung, *et al.*, Dynamic stability of active sites in hydr(oxy)oxides for the oxygen evolution reaction, *Nat. Energy*, 2020, **5**(3), 222–230, DOI: [10.1038/s41560-020-0576-y](https://doi.org/10.1038/s41560-020-0576-y).
- 144 S. Geiger, *et al.*, Catalyst Stability Benchmarking for the Oxygen Evolution Reaction: The Importance of Backing Electrode Material and Dissolution in Accelerated Aging Studies, *ChemSusChem*, 2017, 4140–4143, DOI: [10.1002/cssc.201701523](https://doi.org/10.1002/cssc.201701523).
- 145 S. Geiger, *et al.*, The stability number as a metric for electrocatalyst stability benchmarking, *Nat. Catal.*, 2018, **1**, 508–515, DOI: [10.1038/s41929-018-0085-6](https://doi.org/10.1038/s41929-018-0085-6).
- 146 R. Frydendal, *et al.*, Benchmarking the Stability of Oxygen Evolution Reaction Catalysts: The Importance of Monitoring Mass Losses, *ChemElectroChem*, 2014, **2**, 2075–2081, DOI: [10.1002/celec.201402262](https://doi.org/10.1002/celec.201402262).
- 147 A. Hartig-Weiss, M. F. Tovini, H. A. Gasteiger and H. A. El-Sayed, OER catalyst durability tests using the rotating disk electrode technique: the reason why this leads to erroneous conclusions, *ACS Appl. Energy Mater.*, 2020, **3**(11), 10323–10327, DOI: [10.1021/acsaem.0c01944](https://doi.org/10.1021/acsaem.0c01944).
- 148 H. A. El-Sayed, A. Weiß, L. F. Olbrich, G. P. Putro and H. A. Gasteiger, OER Catalyst Stability Investigation Using RDE Technique: A Stability Measure or an Artifact?, *J. Electrochem. Soc.*, 2019, **166**(8), F458–F464, DOI: [10.1149/2.0301908jes](https://doi.org/10.1149/2.0301908jes).
- 149 A. Moysiadou and X. Hu, Stability profiles of transition metal oxides in the oxygen evolution reaction in alkaline medium, *J. Mater. Chem. A*, 2019, **7**(45), 25865–25877, DOI: [10.1039/c9ta10308b](https://doi.org/10.1039/c9ta10308b).
- 150 E. Fabbri and T. J. Schmidt, Oxygen Evolution Reaction: The Enigma in Water Electrolysis, *ACS Catal.*, 2018, **8**, 9765–9774, DOI: [10.1021/acscatal.8b02712](https://doi.org/10.1021/acscatal.8b02712).
- 151 L. Calvillo, *et al.*, Insights into the durability of Co–Fe spinel oxygen evolution electrocatalysts via operando studies of the catalyst structure, *J. Mater. Chem.*, 2018, **6**, 7034–7041, DOI: [10.1039/C7TA10892C](https://doi.org/10.1039/C7TA10892C).
- 152 L. Francàs, *et al.*, Spectroelectrochemical study of water oxidation on nickel and iron oxyhydroxide electrocatalysts, *Nat. Commun.*, 2019, **10**(1), 5208, DOI: [10.1038/s41467-019-13061-0](https://doi.org/10.1038/s41467-019-13061-0).
- 153 M. Favaro, *et al.*, Understanding the Oxygen Evolution Reaction Mechanism on CoOx using Operando Ambient-Pressure X-ray Photoelectron Spectroscopy, *J. Am. Chem. Soc.*, 2017, **139**(26), 8960–8970, DOI: [10.1021/jacs.7b03211](https://doi.org/10.1021/jacs.7b03211).
- 154 L. Trotochaud, J. K. Ranney, K. N. Williams and S. W. Boettcher, Solution-Cast Metal Oxide Thin Film Electrocatalysts for Oxygen Evolution, *J. Am. Chem. Soc.*, 2012, **134**, 17253–17261, DOI: [10.1021/ja307507a](https://doi.org/10.1021/ja307507a).
- 155 P. P. Lopes, *et al.*, Dynamically stable active sites from surface evolution of perovskite materials during the oxygen evolution reaction, *J. Am. Chem. Soc.*, 2021, **143**(7), 2741–2750, DOI: [10.1021/jacs.0c08959](https://doi.org/10.1021/jacs.0c08959).
- 156 G. Li, L. Anderson, Y. Chen, M. Pan and P. Y. Abel Chuang, New insights into evaluating catalyst activity and stability for oxygen evolution reactions in alkaline media, *Sustainable Energy Fuels*, 2018, **2**(1), 237–251, DOI: [10.1039/c7se00337d](https://doi.org/10.1039/c7se00337d).
- 157 S. Kim, Y. Inoishi, A. Yamanaka, J. T. Song, A. Takagaki and T. Ishihara, Synthesis of Mesoporous NiCo<sub>2</sub>O<sub>4</sub> By Spray Pyrolysis Method for Air Electrode of Zinc–air Rechargeable Batteries, *ECS Meeting Abstracts*, 2020, **MA2020-02**, 394, DOI: [10.1149/MA2020-022394mtgabs](https://doi.org/10.1149/MA2020-022394mtgabs).
- 158 F. Zasada, *et al.*, Periodic DFT and HR-STEM studies of surface structure and morphology of cobalt spinel nanocrystals. Retrieving 3D shapes from 2D images, *J. Phys. Chem. C*, 2011, **115**(14), 6423–6432, DOI: [10.1021/jp200581s](https://doi.org/10.1021/jp200581s).
- 159 S. B. Scott, *et al.*, The low overpotential regime of acidic water oxidation part II: trends in metal and oxygen stability numbers, *Energy Environ. Sci.*, 2022, 1988–2001, DOI: [10.1039/d1ee03915f](https://doi.org/10.1039/d1ee03915f).
- 160 D. B. Trimarco, *et al.*, Enabling real-time detection of electrochemical desorption phenomena with sub-monolayer sensitivity, *Electrochim. Acta*, 2018, **268**, 520–530, DOI: [10.1016/j.electacta.2018.02.060](https://doi.org/10.1016/j.electacta.2018.02.060).
- 161 K. Ehelebe, D. Seeberger, M. T. Y. Paul, K. J. J. Mayrhofer, S. Cherevko and S. Thiele, Evaluating Electrocatalysts at Relevant Currents in a Half-Cell: The Impact of Pt Loading on Oxygen Reduction Reaction Evaluating Electrocatalysts at Relevant Currents in a Half-Cell: The Impact of Pt Loading on Oxygen Reduction Reaction, *J. Electrochem. Soc.*, 2019, **166**(16), F1259–F1268, DOI: [10.1149/2.0911915jes](https://doi.org/10.1149/2.0911915jes).
- 162 J. Knöppel, *et al.*, On the limitations in assessing stability of oxygen evolution catalysts using aqueous model electrochemical cells, *Nat. Commun.*, 2021, **12**(1), 1–9, DOI: [10.1038/s41467-021-22296-9](https://doi.org/10.1038/s41467-021-22296-9).

